ANL-AMMT-013

FY24 Integrated Results for High-Temperature Mechanical Testing of LPBF 316H Stainless Steel

Nuclear Science and Engineering Division

About Argonne National Laboratory

Argonne is a U.S. Department of Energy laboratory managed by UChicago Argonne, LLC under contract DE-AC02-06CH11357. The Laboratory's main facility is outside Chicago, at 9700 South Cass Avenue, Lemont, Illinois 60439. For information about Argonne
and its pioneering science and technology programs, see www.anl.gov.

ANL-AMMT-013

FY24 Integrated Results for High-Temperature Mechanical Testing of LPBF 316H Stainless Steel

---

Prepared by

Xuan Zhang, Yiren Chen, Srinivas Aditya Mantri, Lin Gao, Ed Listwan, Joe Listwan
Argonne National Laboratory

Michael McMurtrey, Ninad Mohale
Idaho National Laboratory

Caleb Massey
Oak Ridge National Laboratory

September 2024

ABSTRACT

This report provides the mechanical test data of laser powder bed fusion (LPBF) 316H stainless steel (SS) collected during Fiscal Year 2024 (FY 24) under the US Department of Energy, Office of Nuclear Energy's Advanced Materials and Manufacturing Technologies program, along with the current state of microstructural-based understandings of the behaviors. Materials with variabilities in manufacturing site, machine, laser parameters, powder chemistry, porosity, specimen geometry and heat treatment were tested in high-temperature tension, creep, fatigue and creep-fatigue. Electron microscopy and optical microscopy were performed on selected materials before and after the tests to provide microstructural-based understandings to the mechanical behavior. It was discovered that the as-built (AB) and stress-relieved (SR) materials exhibit similar behaviors in tension and creep, as do the solution-annealed (SA) and hot-isostatic pressed (HIP) materials. The AB and SR materials are softer but more ductile than the SA and HIP materials in tension. In creep, the LPBF materials have comparable rupture times but lower rupture strains compared to the wrought materials. The AB and SR materials have low creep rupture strains (<10%) when tested at 720°C and 800°C, while the SA and HIP materials are much more ductile. The LPBF materials exhibit large scatter in fatigue and creep-fatigue lives. The cyclic lives of creep-fatigue tests are lower than those of fatigue tests. In fatigue and creep-fatigue, SR materials outperform SA materials. A common observation from the cyclic tests is that, given the same post-build heat treatment, a lower initial peak stress generally results in a longer cyclic life regardless of hold time. It was also discovered that the batch variation can be more impactful than heat treatment, as demonstrated by the overall better performance of one batch of material than another, regardless of the heat treatment. The results provided insights into how different factors impact the behaviors of LPBF 316H SS. An outlook to FY 25 work scope is provided.

TABLE OF CONTENTS

LIST OF TABLES

LIST OF FIGURES

1 Introduction

Advanced materials are a key element in the development and deployment of the next generation nuclear energy systems. The DOE-NE's Advanced Materials and Manufacturing Technologies (AMMT) program aims to accelerate the development, qualification, demonstration, and deployment of advanced materials and manufacturing technologies to enable reliable and economical nuclear energy [1]. A current focus of the AMMT program is to establish a rapid qualification framework, using the qualification of 316H stainless steel (SS) produced by laser powder bed fusion (LPBF) under the American Society of Mechanical Engineers (ASME) Boiler and Pressure Vessel Code (BPVC) Section III, Division 5 for high-temperature reactor Class A construction as a pilot case.

The ASME BPVC qualification of LPBF 316H SS requires the generation of a comprehensive mechanical property database, including high-temperature tension, creep, fatigue, and creep-fatigue. Those data provide the necessary information for constructing the design models. Traditionally, such a database takes 10+ years to generate, largely constrained by the duration of creep tests. A rapid qualification should mitigate this problem by being able to make valid predictions of long-term creep performance with short-term test data. To do so, a thorough understanding of the process-microstructure-property correlation is required.

This report provides the first set of mechanical test data of LPBF 316H SS collected during FY 24 under the AMMT program, along with the current state of microstructural-based understandings of the behaviors. The specimens were made from various materials produced by different LPBF systems located in Argonne National Laboratory (ANL), Oak Ridge National Laboratory (ORNL) and Los Alamos National Laboratory (LANL). The as-built (AB) materials were subjected to different post-build heat treatments including stress relieving (SR), solution annealing (SA) and hot-isostatic pressing (HIP). The tests included high-temperature tension, creep, fatigue, and creep-fatigue, performed by ANL and Idaho National Laboratory (INL). Electron microscopy and optical microscopy were performed on selected materials before and after the tests. The results from those scoping tests and the preliminary characterizations provided insights into how different factors, such as machines, laser parameters, powder chemistry, built-in porosity, and heat treatment, impact the materials behaviors. An outlook to FY 25 work scope is also provided.

2 Materials and methods

2.1 Materials

Five batches of 316H SS powders have been acquired under the AMMT program, as listed in Table 2.1. Four were from Praxiar Inc. (currently Linde plc), labeled as Prax-AM316H-1 to Prax-AM316H-4, and one was from Powder Alloy Corporation (PAC), labeled as PAC-AM316H-1. Their compositions, as provided by the manufacturers (Table 2.1), are within the range of UNS S31609 (316H SS) as specified in ASTM A213/A213M [2].

Table 2.1. Chemical compositions of powders utilized in this study.

		ASTM UNS S31609	**316H powder**	**316H powder**	**316H powder**	**316H powder**	**316H powder**
Manufacturer			Praxair	Praxair	Praxair	Praxair	PAC
Designation		--	Prax-AM316H-1	Prax-AM316H-2	Prax-AM316H-3	Prax-AM316H-4	PAC-AM316H-1
Order quantity (kg)		- -	50	200	500	1000	200
Build designation			Not used in this study	ANL-B1; ORNL-ANL-best	ANL-B2; ORNL-B1; ORNL-B2	LANL-B2	LANL-B1
Composition (wt.%)	**Fe**	Bal.	Bal.	Bal.	Bal.	Bal.	Bal.
	Cr	16.0-18.0	17.6	16.8	17.0	16.7	16.94
	Ni	11.0-14.0	12.3	12.1	12.3	11.9	10.88
	Mo	2.00-3.00	2.6	2.5	2.3	2.6	2.23
	Mn	2.0*	1.03	1.13	1.05	0.02	1.02
	Si	1.00*	0.41	0.48	0.07	0.04	0.37
	C	0.04-0.10	0.05	0.06	0.08	0.07	0.043
	O	- -	0.05	0.03	0.03	0.02	0.048
	N	- -	0.01	0.01	0.01	0.01	0.05
	P	0.045*	<0.005	<0.005	<0.005	<0.005	0.031
	S	0.030*	0.00	0.00	0.00	0.00	0.001

* Maximum, unless a range or minimum is indicated.

The materials were printed with different laser systems, namely Renishaw AM400, GE Concept Laser, and EOS M290. The machine, site, laser mode and printing parameters are listed in Table 2.2. The designations of corresponding builds are also provided.

Table 2.2. The machine, site, build designation, laser mode and printing parameters used in this study.

Lab/ machine	Build designation	Laser mode	Laser Power (W)	Spot size (µm)	Scan speed (m/s)	Hatch spacing (µm)	Layer height (µm)	Rotation angle (°)	Energy density (J/mm^3)
ANL/Renishaw AM400	ANL-B1; ANL-B2	Pulsed	195	70	0.67	110	50	67	53
ORNL/GE Concept Laser	ORNL-B1	Continuous	200	125	0.75	75	50	67	71
ORNL/GE Concept Laser	ORNL-B2	Continuous	290	130	1.5	75	50	67	52
ORNL/Renishaw AM400	ORNL-ANL-best	Pulsed	195	70	0.67	110	50	67	53
ORNL/Renishaw AM400	ORNL-ORNL-best	Pulsed	200	70	0.58	90	50	67	76
LANL/EOS M290	LANL-B2	Continuous	275	100	0.69	140	30	47	95

Table 2.3 lists the parameters of post-build heat treatments used in this study. Figure 2.1 shows the work flow in obtaining the test specimens. All specimens in this study have their longitudinal directions parallel to the build direction (BD).

Table 2.3. Parameters of post-build heat treatments used in this study.

Heat treatment	Temperature	Time	Quench	Pressure
Stress relieving (SR)	650° C	24 hour	Furnace/air	n/a
Solution annealing (SA)	1100° C	1 hour	Water	n/a
Hot isostatic pressing (HIP)	1120° to 1163° C	4 hours	Cool in inert atmosphere	≥100 MPa

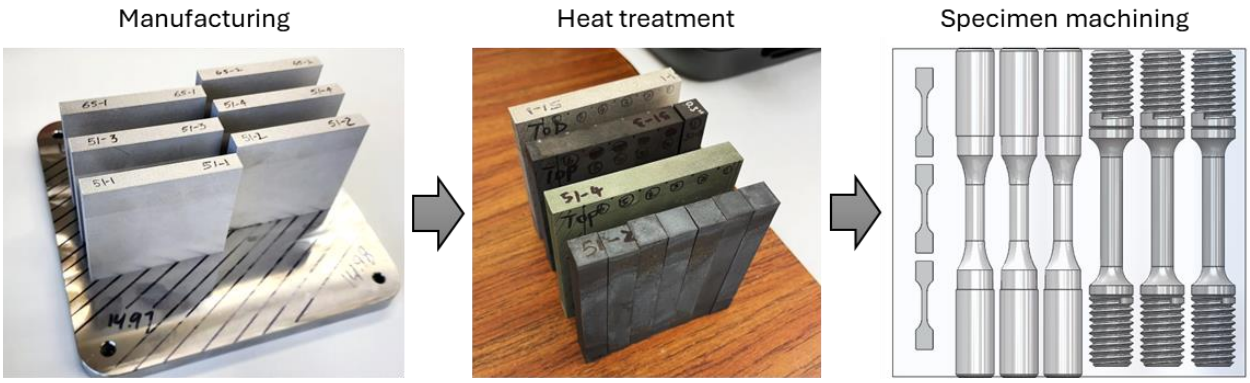

Figure 2.1. The work flow in obtaining the test specimens.

2.2 Tension tests

Tension tests of subsized specimens were performed with two Instron Model 5980 Materials Testing Systems with the Instron Bluehill 3 testing software for control and data acquisition. Figure 2.2 provides the specimen dimensions. The testers are equipped with 3-zone furnaces for air testing up to 1100°C. To begin a test, a specimen was installed into a grip that was designed for shoulder loading. The tips of two thermal couples were placed in close vicinity to the top and bottom region of the gauge section of the specimen to reflect the actual temperature of the specimen and to serve as the input of the furnace control. The temperature was brought up to the target gradually and a soaking period of 1 hour was applied to ensure a thermal equilibrium of the loading train. All tests were conducted with a crosshead displacement rate of 0.00762 mm/s until rupture. The elastic modulus of the raw data was corrected with the known values of E = 200 GPa, 155 GPa, 146 GPa, and 134 GPa for 316 SS at RT, 550, 650 and 750°C, respectively [3].

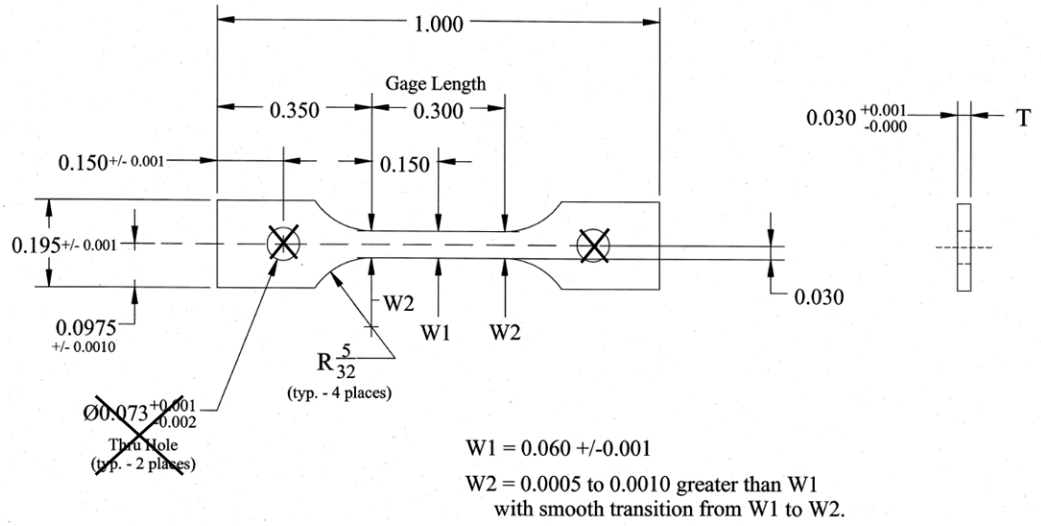

Figure 2.2. Subsized SS-3 type tension specimen geometry. The two pin holds are not machined for the specimens used in this study and are thus crossed out.

2.3 Creep tests

At ANL, the creep tests were performed in the Mechanical and Environmental Testing Laboratory and were conducted in accordance with ASTM E139 "Standard Test Methods for Conducting Creep, Creep Rupture, and Stress Rupture Tests of Metallic Materials". Figure 2.3 (a) shows a photograph of the lab, and Figure 2.3 (b) shows the specimen geometry. The frames were ATS Series 2300 Lever Arm Creep Testing Systems integrated with WinCCS II computer control and data acquisition software package. ATS systems are precision knife-edge lever arm testers. Each creep machine is equipped with a three-zone split-tube furnace capable of operation up to 1100°C. The temperature in the system is controlled by the ATS temperature control system which regulates the power applied to the resistive heating elements and maintains the desired temperature (setpoint) as measured by a control thermocouple. Type K thermocouples are used to measure the specimen temperatures, and when doing so, the two thermocouples are spot welded to the shoulder sections of the specimen and fed into the furnace control.

At INL, similarly, creep tests were conducted in accordance with ASTM E139 on Applied Test Systems lever arm creep frames, using a three-zone furnace for temperature control. For standard

specimen testing, cylindrical test specimens similar to Figure 2.3 (b) were used with the longitudinal direction parallel to the build direction. Specimens had a 6.35-mm [0.250 in.] minimum diameter and a reduced parallel section that was at minimum 31.75-mm [1.250 in]. A modified test specimen geometry was used for sub-sized specimen testing that had a rectangular cross section that was 1.2 mm [0.047 in.] wide and either 0.5 mm [0.0197 in.] or 0.75 mm [0.0295 in.] thick. The reduced parallel section was 5 mm [0.197 in.] long.

(a)

(b)

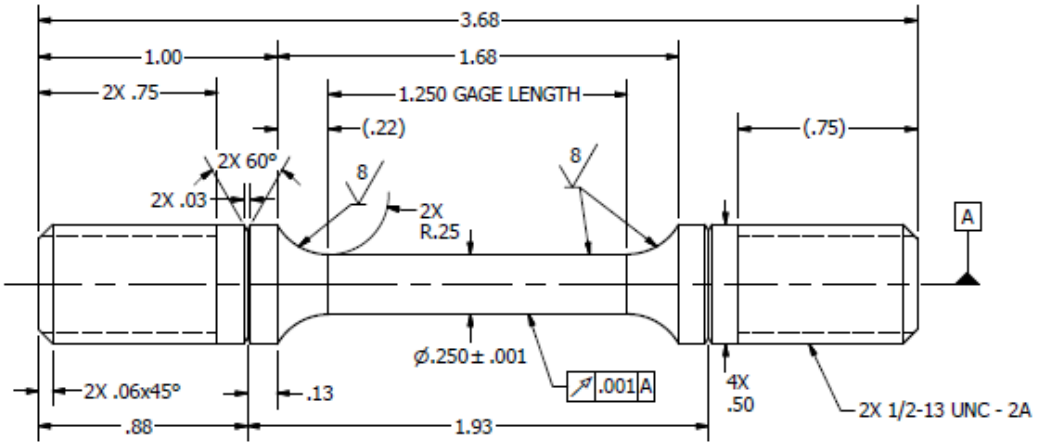

Figure 2.3. (a) Creep lab in ANL; (b) Dimensions of ANL creep specimens in ASTM standard geometry.

2.4 Fatigue/creep-fatigue tests

Fatigue and creep-fatigue tests were performed at ANL and INL on different AM builds in this study. While each laboratory used its own sample types and loading frames, the same test protocols and ASTM standards were followed for fatigue and creep tests as shown in Table 2.4. At ANL, a round bar specimen with a nominal gauge diameter of 5.5 mm (0.215 in.), a gauge length of 16.3

mm (0.64 in.), and a total length of 101.6 mm (4.0 in.), as shown in Figure 2.4, were used. Tests were carried out on two closed-loop servo-hydraulic test frames. Specimen heating was provided by two three-zone split furnaces. The test temperature was controlled and monitored with two pairs of Type K thermocouples positioned at the top and bottom grip sections of the specimen. All the tests were conducted at 550°C in air. The fatigue tests were carried out under a constant strain amplitude in a fully reversed (R = -1) mode. A high-temperature extensometer was mounted at the uniform gauge section of the specimen to control the test. Both tension and compression strain rates were set at 0.001 s^{-1}. Creep-fatigue tests were performed using the same test systems and the same sample geometry as those used in the fatigue tests. To induce creep deformation, a hold time was applied at the peak tensile strain for each cycle. Instron WaveMatrix^{TM} Dynamic Software was used for test control and data acquisition. Stress-strain hysteresis loops and the maximum and minimum stresses were recorded periodically at different cycles throughout the test.

At INL, fatigue and creep-fatigue tests were performed on several MTS servo-hydraulic test frames, using three-zone furnaces for temperature control. The tests were also conducted in a strain-controlled mode with a fully reversed (R = -1) strain range of 1%. A triangular strain wave-form and a strain rate of 0.001 s^{-1} were used for all tests. Cylindrical test specimens were machined with their longitudinal direction parallel to the build direction. Specimens tested at INL had a 7.49-mm (0.29 in.) minimum diameter and a 20.0-mm (0.79 in.) parallel gauge section. The extensometer used at INL had a gauge length of 12 mm (0.47 in.). Creep-fatigue tests were performed using the same specimen geometry and extensometer. The tests were also fully reversed, but a hold time was implemented at peak tensile strain. The cyclic life was defined as the number of cycles when a drop of 20% in the ratio of peak and valley (maximum and minimum) stresses was detected.

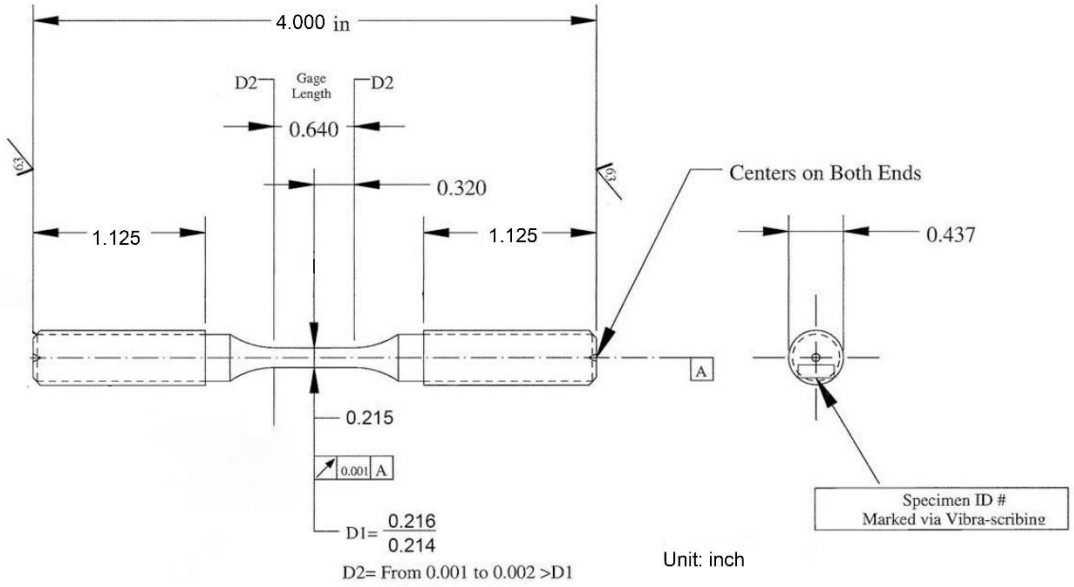

Figure 2.4 Round bar specimens used at ANL for the fatigue and creep-fatigue tests

Table 2.4. Fatigue and creep-fatigue tests performed at ANL and INL

	Sample		Test method	Strain rate	Test standard	
	Gauge length	Gauge dia.			Fatigue	Creep-fatigue
ANL	0.64”	0.215”	Strain controlled, R=-1	0.1%/s	E606/606M	E2714
INL	0.79”	0.29”	Strain controlled, R=-1	0.1%/s	E606/606M	E2714

2.5 Characterization

Scanning electron microscopy (SEM) was performed with a JEOL IT800HL microscope. Specimen surfaces were mechanically polished to mirror finish and final polished with a Buehler VibroMet system in 0.06-μm silica suspension. Electron beam voltages of 5-15 keV were used in those experiments. Both secondary electron detector (SED) imaging and backscattered electron (BSE) imaging were used to highlight different features. Electron backscatter diffraction (EBSD) and energy dispersive x-ray spectroscopy (EDS) were performed on selected specimens to provide quantitative information on grain structures and secondary phases.

Scanning transmission electron microscopy (STEM) in high-angle annular dark field (HAADF) and bright field (BF) imaging modes were performed with a FEI Talos F200X TEM/STEM at the Center for Nanoscale Materials (CNM) in ANL to study the microstructures of selected specimens. Specimens were mechanically polished down to 100 μm in thickness, and 3 mm TEM disks were punched out. The disks were then jet-polished until electron transparent with an electrolyte of 5% perchloric acid and 95% methanol at −30 °C with a Struers TenuPol-5 jet polisher. EDS was used to map the chemical composition of selected areas of interest. The EDS intensity maps were converted to Quantitative Hyperspectral X-ray Maps (Q-maps) for analysis.

3 Tension tests

Uniaxial tension tests were performed at room temperature (RT), 550°C, 650°C and 750°C for ANL-B1 materials in the vertical direction (i.e., along BD) subjected to different heat treatments as specified in Table 2.3. Figure 3.1 shows the engineering stress-strain curves. A general observation is that the AB and SR materials behave similarly, as do the SA and HIP materials. The more aggressive heat treatment from SA & HIP puts the material's tensile behavior closer to that of the wrought, but appreciable differences still exist in that the wrought material is softer and has higher strain hardening capability at all temperatures. At 550°C and 650°C where the dynamic strain aging (DSA) is observed, the DSA is more pronounced in SA and HIP materials compared to that in the AB and SR materials. This can be explained by the fact that the SA and HIP treatments recover the dislocation structure, homogenize the element distribution and put solutes back into solution, and therefore promotes the interaction of mobile solutes like C, O and Cr with mobile dislocations.

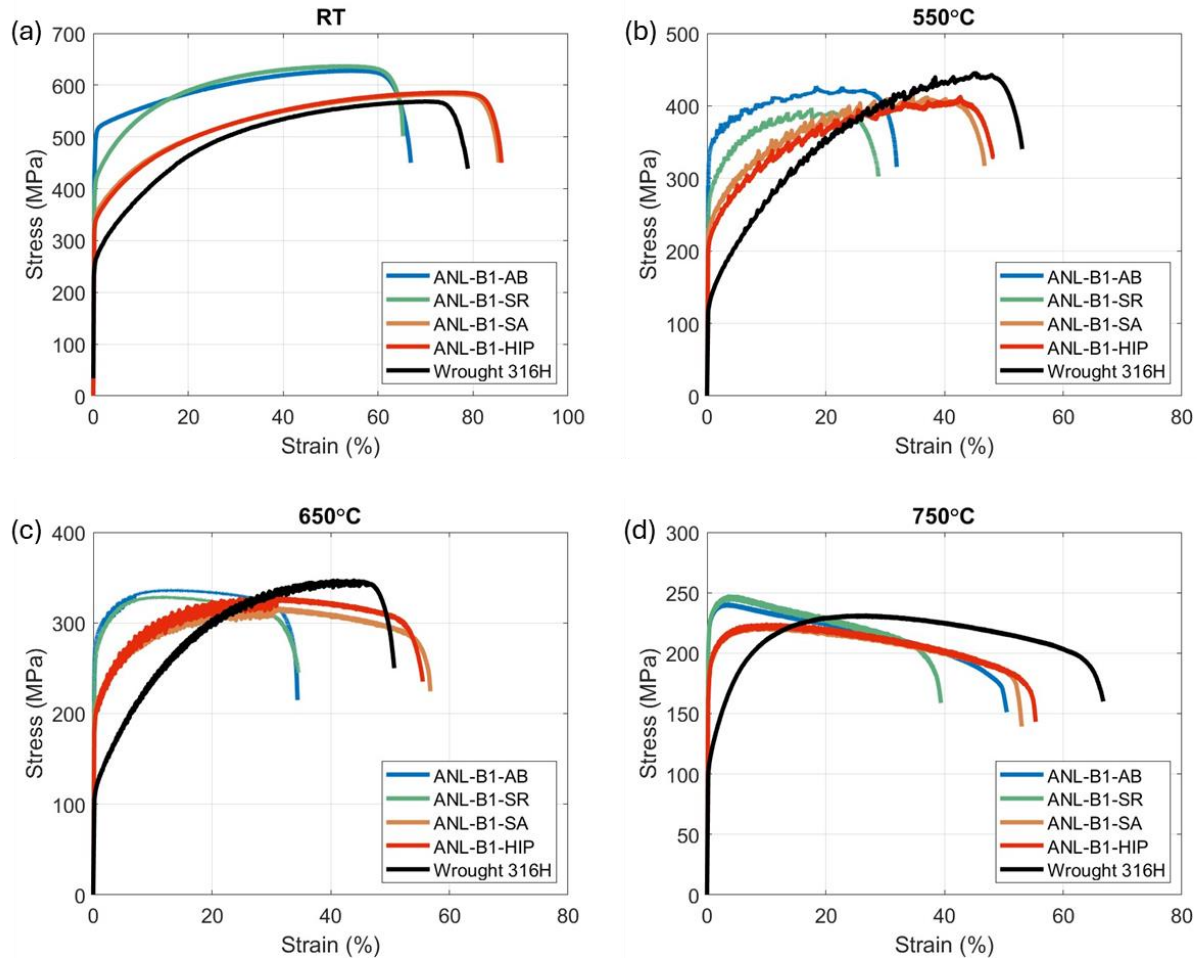

Figure 3.1. Engineering stress-strain curves of ANL-B1 materials in AB, SR, SA and HIP conditions tested at (a) RT, (b) 550°C, (c) 650°C, and (d) 750°C.

Figure 3.2 plots the tensile properties of the materials obtained from the tests in Figure 3.1. As the temperature increases, the yield strength (YS), ultimate tensile strength (UTS) and uniform elongation (UEL) all decreases. The total elongation (TEL) first decreases with temperature and then has an increasing trend above 550°C. Again, the behaviors of AB and SR materials are similar, as are those of SA and HIP materials. The LPBF materials are much stronger in YS compared to the wrought material and are much higher than the ASME design curve. The differences are smaller between heat treatments, the wrought and the design curve in UTS, especially at elevated temperatures. The SA and HIP materials are more ductile than the AB and SR materials and are closer to the wrought.

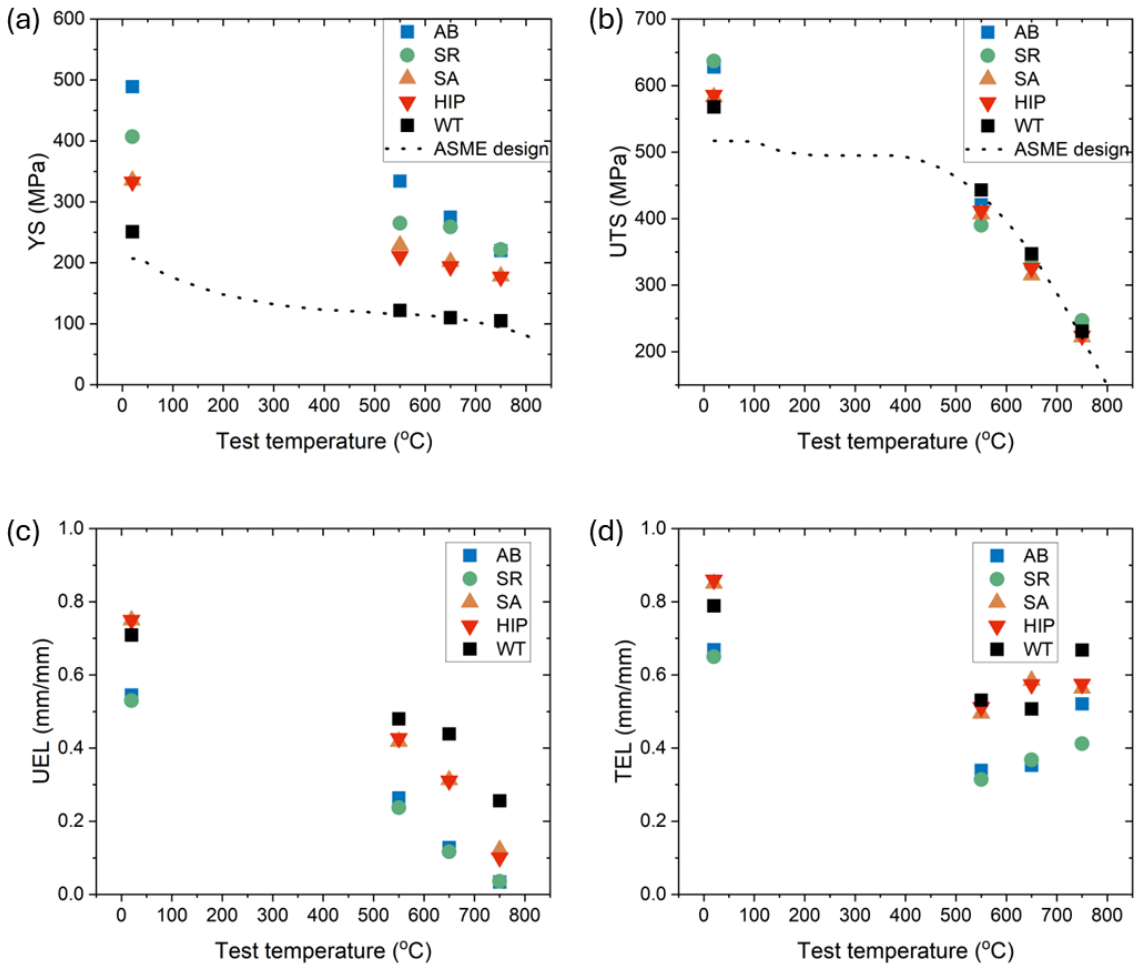

Figure 3.2. Tensile properties of ANL-B1 materials in AB, SR, SA and HIP conditions, in comparison to the wrought and the ASME design curves. (a) YS; (b) UTS; (c) UEL; (d) TEL.

4 Creep tests

4.1 Creep behavior

The creep ruptures in FY 24 are presented in Table 4.1. A total of 34 rupture tests were completed, with rupture times ranging from 69 to 2254 h. Sections 4.1.1 and 4.1.2 describe the creep curves and the creep properties, respectively.

Table 4.1. Conditions of ruptured creep tests in FY 24.

Build	Heat treatment	Specimen geometry	Orientation	Status	Temperature (°C)	Stress (MPa)
Wrought	SA	Standard	Along BD	Ruptured	725	100
ANL-B1	AB	Standard	Along BD	Ruptured	600	248
ANL-B1	SR	Standard	Along BD	Ruptured	600	248
ANL-B1	SA	Standard	Along BD	Ruptured	600	248
ANL-B1	HIP	Standard	Along BD	Ruptured	600	248
ANL-B1	AB	Standard	Along BD	Ruptured	725	100
ANL-B1	SR	Standard	Along BD	Ruptured	725	100
ANL-B1	SA	Standard	Along BD	Ruptured	725	100
ANL-B1	HIP	Standard	Along BD	Ruptured	725	100
ANL-B1	AB	Standard	Along BD	Ruptured	800	53.3
ANL-B1	SR	Standard	Along BD	Ruptured	800	53.3
ANL-B1	SA	Standard	Along BD	Ruptured	800	53.3
ANL-B1	HIP	Standard	Along BD	Ruptured	800	53.3
ANL-B2	SR	Standard	Along BD	Ruptured	600	248
ANL-B2	SR	Standard	Along BD	Ruptured	725	100
ANL-B2	SR	Standard	Along BD	Ruptured	800	53.3
ORNL-B1	SR	Standard	Along BD	Ruptured	600	248
ORNL-B1	SA	Standard	Along BD	Ruptured	600	248
ORNL-B1	HIP	Standard	Along BD	Ruptured	600	248
ORNL-B1	SR	Standard	Along BD	Ruptured	725	100
ORNL-B1	SA	Standard	Along BD	Ruptured	725	100
ORNL-B1	HIP	Standard	Along BD	Ruptured	725	100
ORNL-B2	SR	Standard	Along BD	Ruptured	600	248
ORNL-B2	SA	Standard	Along BD	Ruptured	600	248
ORNL-B2	HIP	Standard	Along BD	Ruptured	600	248
ORNL-B2	SR	Standard	Along BD	Ruptured	725	100
ORNL-B2	SA	Standard	Along BD	Ruptured	725	100
ORNL-B2	HIP	Standard	Along BD	Ruptured	725	100
ORNL-ANL-best	SR	Standard	Along BD	Ruptured	600	248
LANL-B2	SR	Standard	Along BD	Ruptured	600	248
ORNL-B1	SR	Subsized, SS-J2	Along BD	Ruptured	600	248
ORNL-B1	SR	Subsized, SS-J3	Along BD	Ruptured	600	248

ORNL-B1	SR	Subsized, SS-J2	Along BD	Ruptured	725	100
ORNL-B1	SR	Subsized, SS-J3	Along BD	Ruptured	725	100

4.1.1 Creep curves

The various material/test condition combinations provided different perspectives in evaluating the creep performance of LPBF 316H SS. This section describes the creep curves and the observations made from them.

Effect of heat treatment: Figure 4.1 and Figure 4.2 plot the creep curves of materials from ANL-B1 and ORNL-B1 builds subjected to different heat treatments as listed in Table 2.3. Both builds were manufactured with optimized printing parameters and have very low porosities (0.03-0.06%). Tests under the same conditions were grouped and shifted along the time axis for better visualization. For the 725°C, 100 MPa condition, the curve from a wrought material was added.

While there are many differences among the materials and test conditions, there are a few common observations. First, the LPBF materials behave very differently from the wrought material at 725°C, 100 MPa with extended secondary creep stages and reduced rupture strains. Second, the SA and the HIP materials behave similarly at all test conditions; the same for the AB and the SR materials. Third, the SA and HIP materials have similar or higher rupture strains compared to the AB and SR materials. Particularly, under 725°C, 100 MPa, the AB and SR materials have very low rupture strains (< 10%) while the SA and HIP materials are much more ductile.

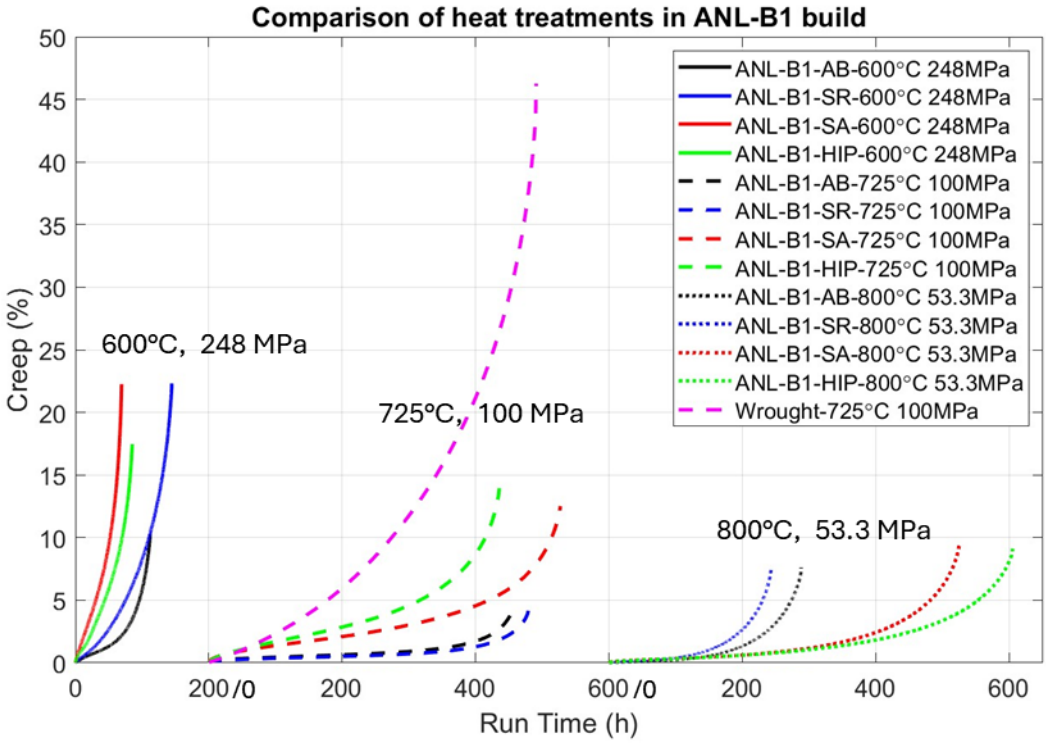

Figure 4.1. Creep curves of ANL-B1 materials subjected to different heat treatment under various test conditions.

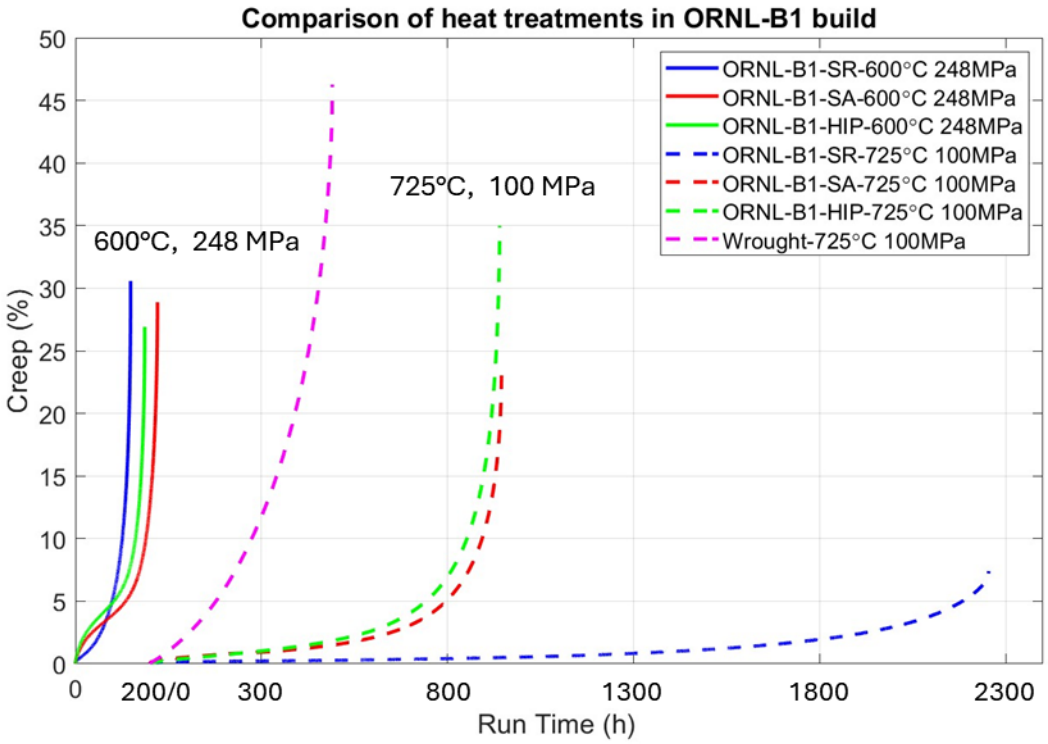

Figure 4.2. Creep curves of ORNL-B1 materials subjected to different heat treatment under various test conditions.

Effect of chemistry: Comparing the ANL-B1 and ANL-B2 builds (Table 2.1 and Table 2.2), the only difference is the powder chemistry, particularly in Si and C. For ANL-B1, Si is 0.48 wt.% and C is 0.06 wt.%. For ANL-B2, Si is 0.07 wt.% and C is 0.08 wt.%. Figure 4.3 shows the creep curves of materials in the SR state from the two builds under various test conditions. In general, ANL-B2 outperforms ANL-B1, with lower creep rates, longer rupture times and moderately better rupture strains. Tests on SA materials will be performed in FY 25 to see if the same trend can be observed.

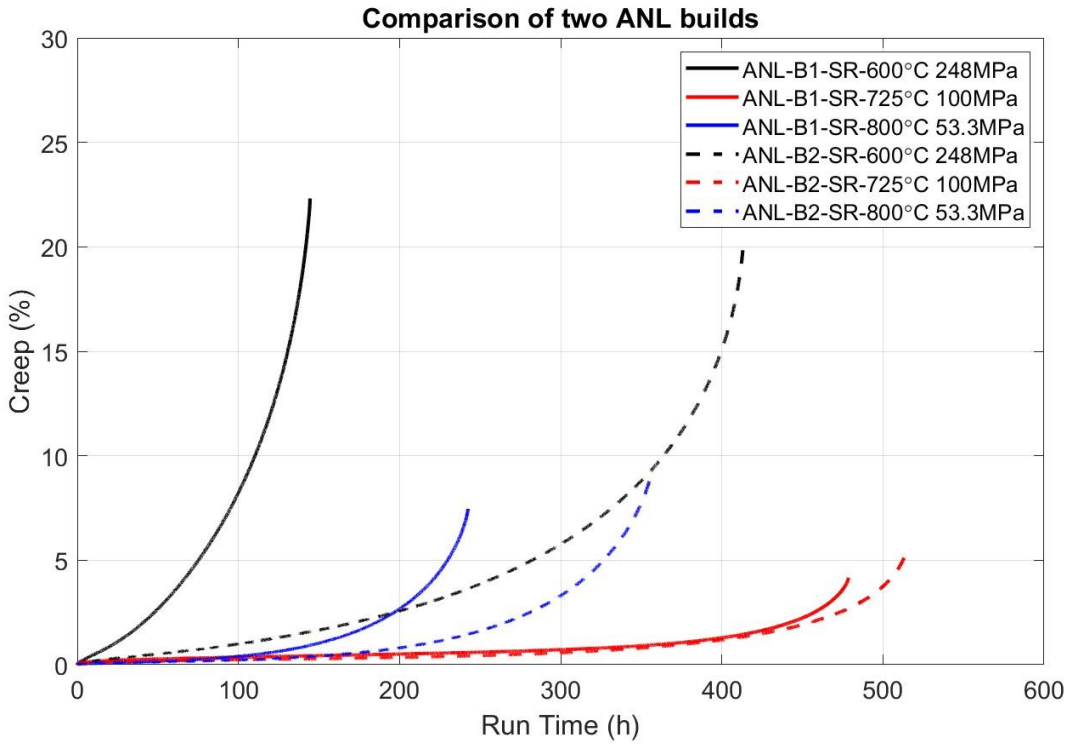

Figure 4.3. Creep curves of ANL-B1 and ANL-B2 materials in stress-relieved state under various test conditions.

Effect of porosity: Comparing the ORNL-B1 and ORNL-B2 builds (Table 2.1 and Table 2.2), they used the same batch of powder but were printed with different laser parameters, resulting in different levels of porosity: ORNL-B1 is ~0.03% while ORNL-B2 is ~0.3% (Figure 4.4). The creep curves of materials from those two builds subjected to different heat treatments are plotted in Figure 4.5. It is seen that systematically, ORNL-B2 has lower rupture strains for a certain heat treatment condition under a certain test condition. Under 725°C, 100 MPa, ORNL-B1-SR significantly outperformed ORNL-B2-SR with a longer rupture time, a lower minimum creep rate and a higher rupture strain. This may imply that a higher porosity can significantly degrade creep performance, yet differences in other microstructural features need to be evaluated. An interesting observation is that the difference between ORNL-B1-HIP and ORNL-B2-HIP is similar to that between ORNL-B1-SA and ORNL-B2-SA. However, both HIP materials have minimal porosity as seen in Figure 4.4, while the ORNL-B2-SA has much higher porosity level than the ORNL-B1-SA. This result indicates that the effect of porosity is likely secondary (probably mostly on reducing rupture strains); other features, such as the grain structures, may play a more dominant role in determining the time to rupture and the creep rate. More research is needed to clarify the effect of microstructural features on the creep performance in those two sets of materials.

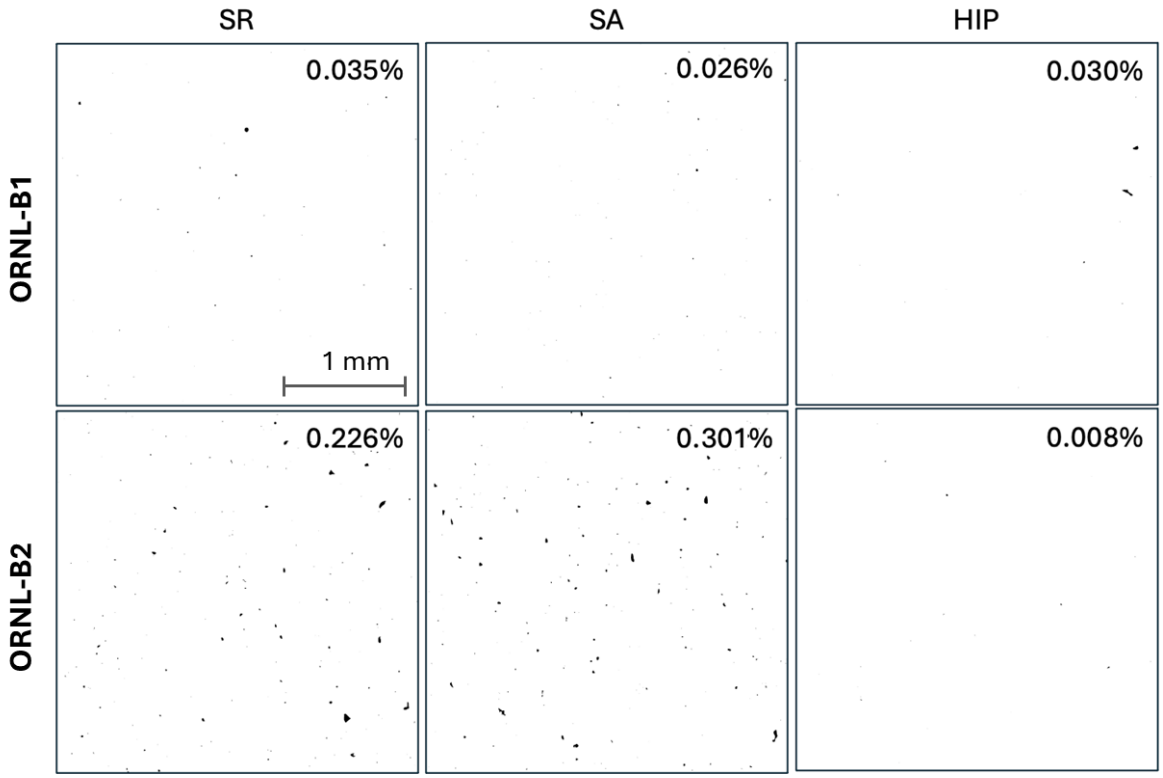

Figure 4.4. Optical micrographs showing the porosity levels in ORNL-B1 and ORNL-B2 builds subjected to different post-build treatments.

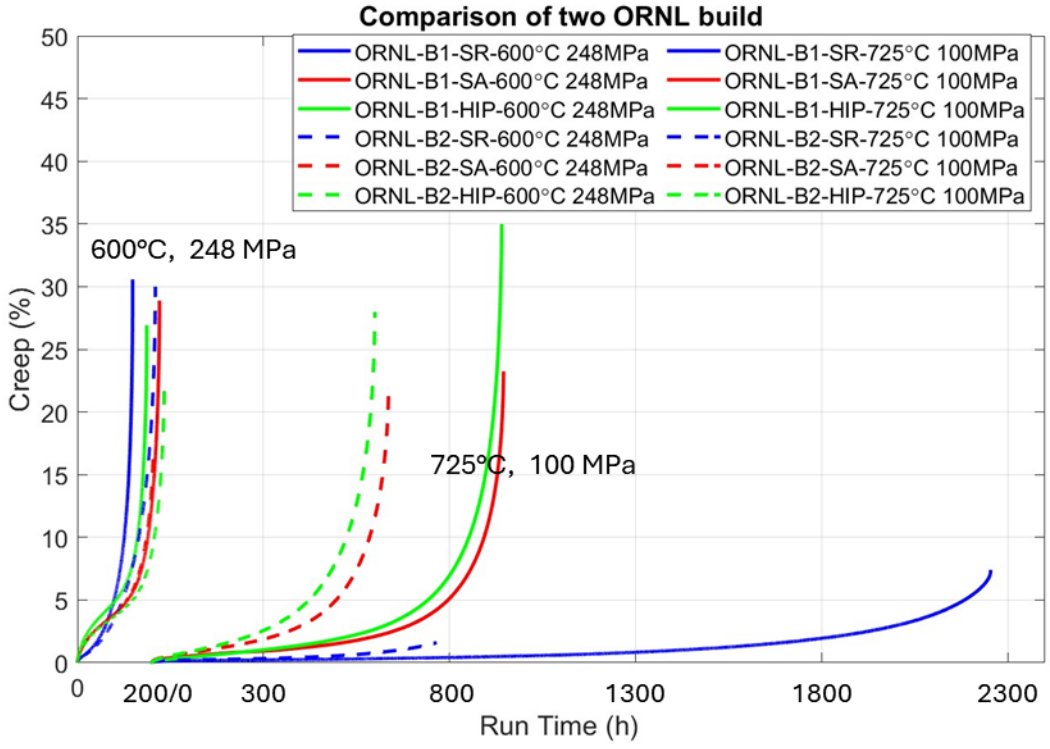

Figure 4.5. Creep curves of ORNL-B1 and ORNL-B2 materials subjected to different heat treatment under various test conditions.

Effect of sample geometry: Two creep tests at 600°C, 248 MPa were performed with ORNL-B1 material machined into sub-sized SS-J geometries. One specimen is 0.75 mm in thickness and the other is 0.5 mm. Their creep curves are plotted in Figure 4.6 along with the curve of a standard sized specimen. Figure 4.7 shows the photos of ruptured sub-size specimens. Both specimens show necking near the failure point, agreeing with the recorded high rupture strains. While the 0.75-mm sub-sized specimen behaves very similarly to the standard sized specimen, the 0.5-mm sub-sized specimen shows a similar minimum creep rate but a much more prominent primary creep stage and a much shorter rupture time. The prominent primary creep stage could have some relation to the uncertainties in accurately deciding when the load was fully applied. The shorter rupture time could be due to the intrinsic variations in creep testing as well as a geometry effect. Repetitive tests will need to be performed to clarify whether the size effect is significant.

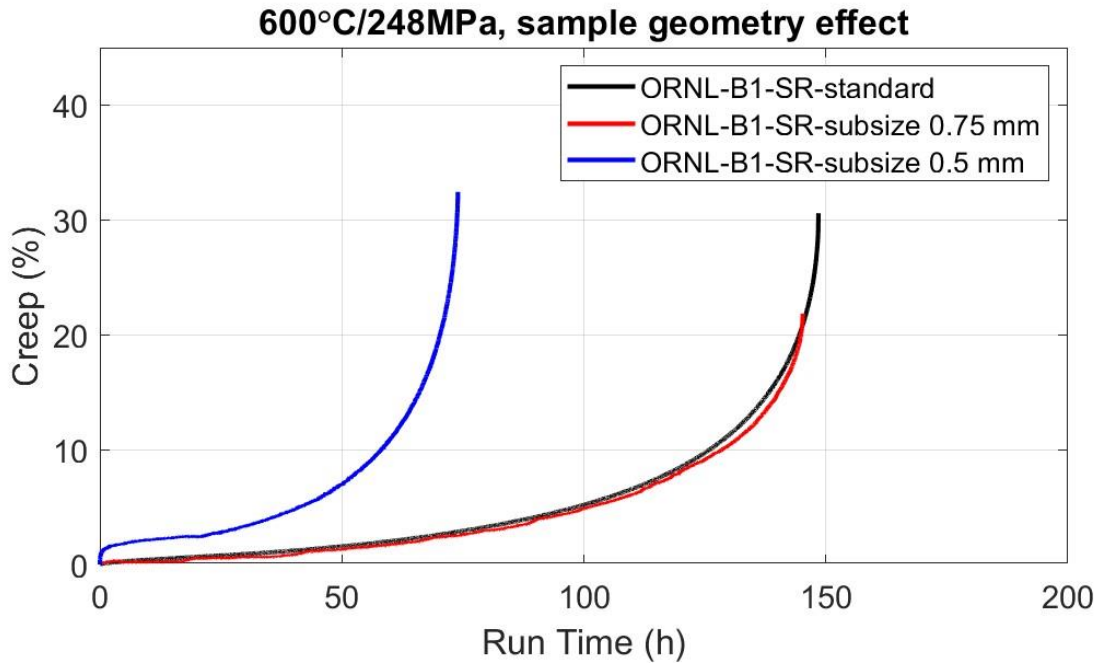

Figure 4.6. Creep curves of ORNL-B1 specimens in different geometries and tested under 600°C, 248 MPa.

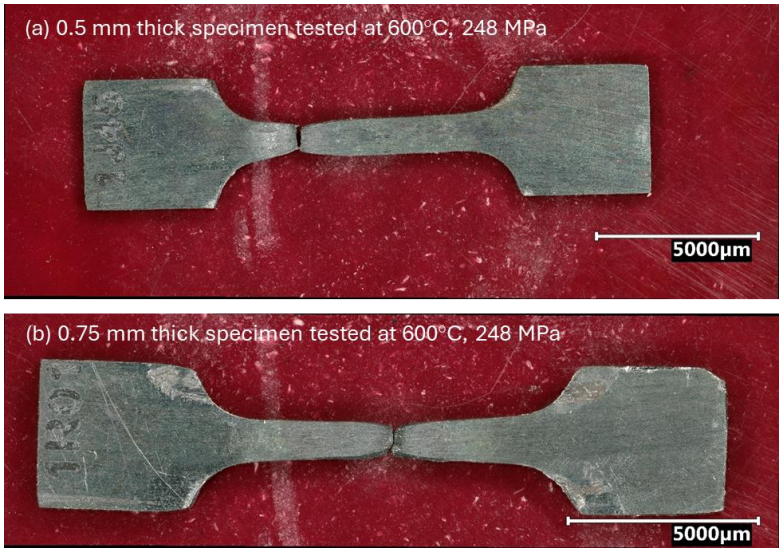

Figure 4.7. Photos of ruptured sub-sized specimens tested under 600°C, 248 MPa. (a) 0.5-mm thick specimen; (b) 0.75-mm thick specimen.

Mixed effect of batch variations: The comprehensive testing (Table 4.1) includes materials manufactured at different sites using different machines and with different batches of powders. Furthermore, the tests may be performed at different sites. Some of the variations are captured in Figure 4.8. All the tests in Figure 4.8 were performed under 600°C, 248 MPa on SR materials. As can be seen, no clear correlation is observed among those factors so far. An interesting finding is with the sample printed by ANL in a solid red line and the sample printed by ORNL in a dotted blue line. Both prints used Renishaw AM400 machines with the same laser parameters, used the same batch of powders (Praxs-AM316H-2), and printed into similar plate geometries. While it is expected that the materials are nearly identical, the creep curves show appreciable differences, perhaps simply due to the intrinsic uncertainty in creep testing. More tests are underway to provide further inputs to the mixed effect of batch variations.

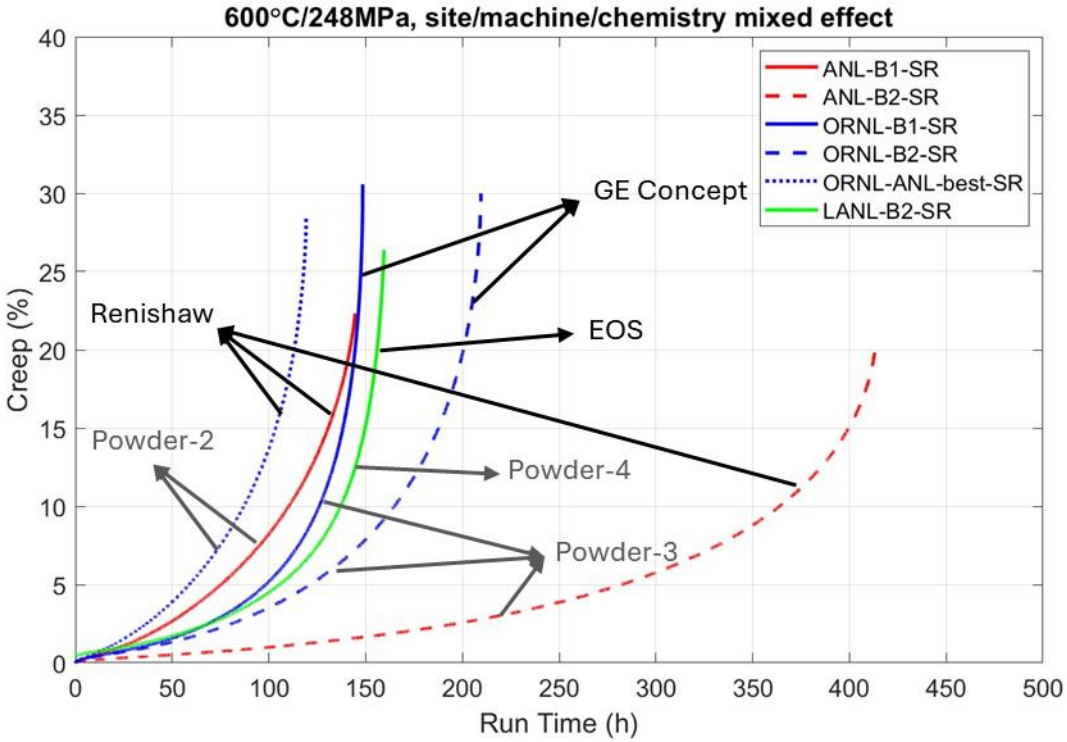

Figure 4.8. Creep curves of various materials in SR state tested under 600°C, 248 MPa.

4.1.2 Creep properties

A comprehensive description of the creep properties of LPBF 316H SS using the data generated under this work is provided in another milestone report [4]. In this section, an overview is provided concerning the behaviors of two categories of materials: AB & SR (category 1), and SA & HIP (category 2). The other variables (printer, site, chemistry, etc.) are not considered. Figure 4.9 is the Larson-Miller plot of the LPBF 316H SS data overlaying the wrought material data gathered from open literature and past DOE reports. The Larson-Miller parameter (LMP) is calculated as

$$LMP = (T + 273.15) \cdot (C + \log(t)),$$

where T is the temperature in °C, C is a constant taken as 16.28 [4], and t is the rupture time. Figure 4.9 shows that both categories of materials are within the scatter band of the wrought materials.

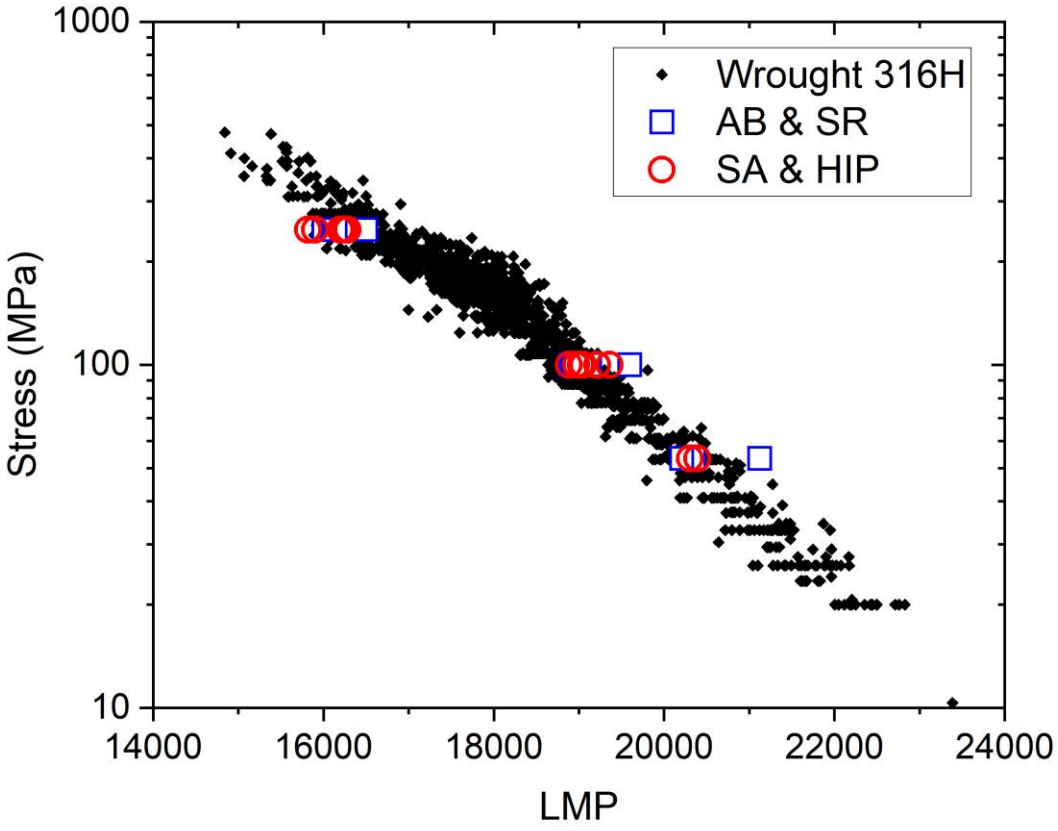

Figure 4.9. Creep rupture data collected to date on LPBF 316H SS compared to the wrought rupture database on a Larson-Miller plot.

Figure 4.10 plots the rupture strains of the LPBF 316H SS tests as a function of temperature. A dashed line at 10% strain is added for visual reference. It is seen that the rupture strains tend to decrease as the temperature increases. When tested at the two higher temperatures, the AB & SR materials tend to have poor creep ductility with rupture strains below 10%. On the other hand, with the more aggressive heat treatment such as SA and HIP, the rupture strains recovered to above 10%. As will be discussed in Section 4.2.1 on specimens circled out in Figure 4.10, it is possible that the heavier precipitation of embrittling phases along the grain boundaries in the AB and SR materials compared to that in the SA and HIP materials is responsible for the reduced creep ductility.

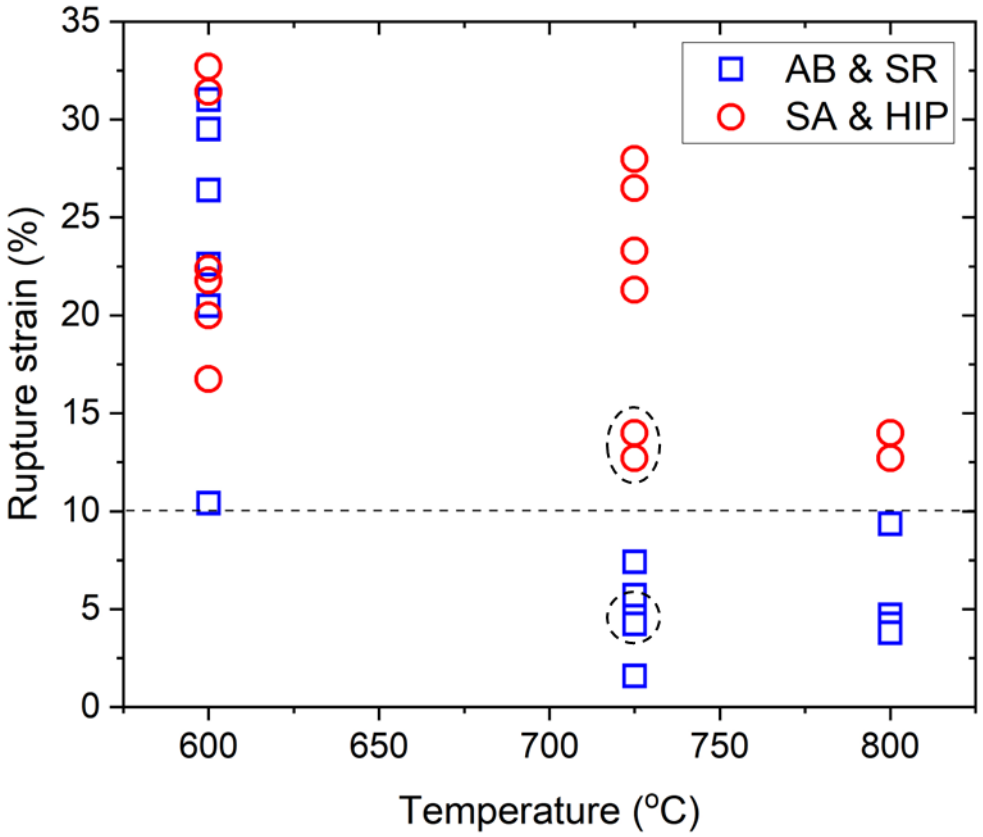

Figure 4.10. Creep ductility data collected for the LPBF 316H materials. The materials of the tests circled out in black were characterized and will be discussed in Section 4.2.1.

4.2 Microstructural observations

While there are many interesting aspects of the creep behavior of LPBF 316H, in FY 24, the microstructural characterization focuses on addressing two topics: 1) the higher creep ductility in the SA & HIP materials compared to the AB & SR materials, and 2) the different creep behavior between the ANL-B1-SR and ORNL-B1-SR materials tested under 725°C, 100 MPa. Figure 4.11 shows how a creep-ruptured specimen was studied. Fractography, SEM and (S)TEM specimens were prepared from different sections of the specimen according to the procedures described in Section 2.5.

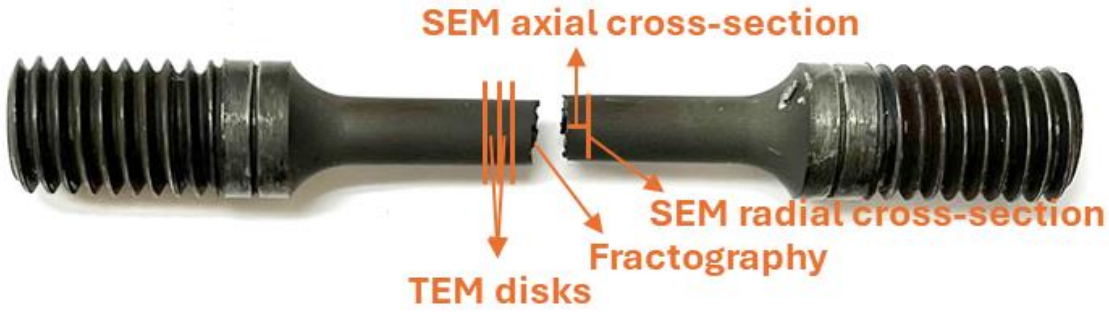

Figure 4.11. Schematics showing how a creep-ruptured specimen was studied.

4.2.1 Effect of heat treatment on creep ductility

Figure 4.12 shows the EBSD IPF maps of the ANL-B1-AB (the same is expected for ANL-B1-SR), ANL-B1-SA and ANL-B1-HIP materials. In the normal to BD direction, the grains have the "chessboard" structure. In the along BD direction, the grains have the "V" shaped structure. Specimens from those materials were creep ruptured under 725°C, 100 MPa. Figure 4.13 and Figure 4.14 shows the fractographic images in low and high magnifications. It is seen that the materials failed by intergranular cracking. In fact, the chessboard structures are visible, indicating that the cracks tend to propagate along grain boundaries across a specific print layer. Only in the HIP specimen, areas showing a somewhat ductile fracture (dimples) are observed (Figure 4.14 bottom right image).

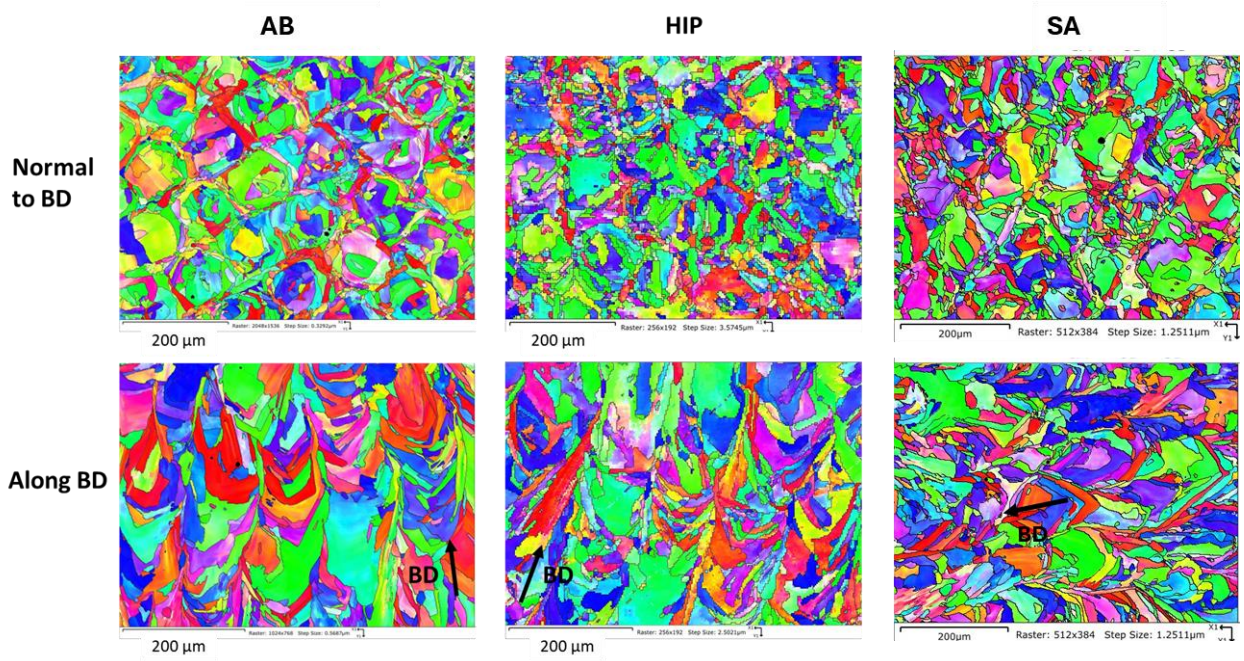

Figure 4.12. EBSD maps showing grain structures in ANL-B1-AB, ANL-B1-HIP and ANL-B1-SA materials.

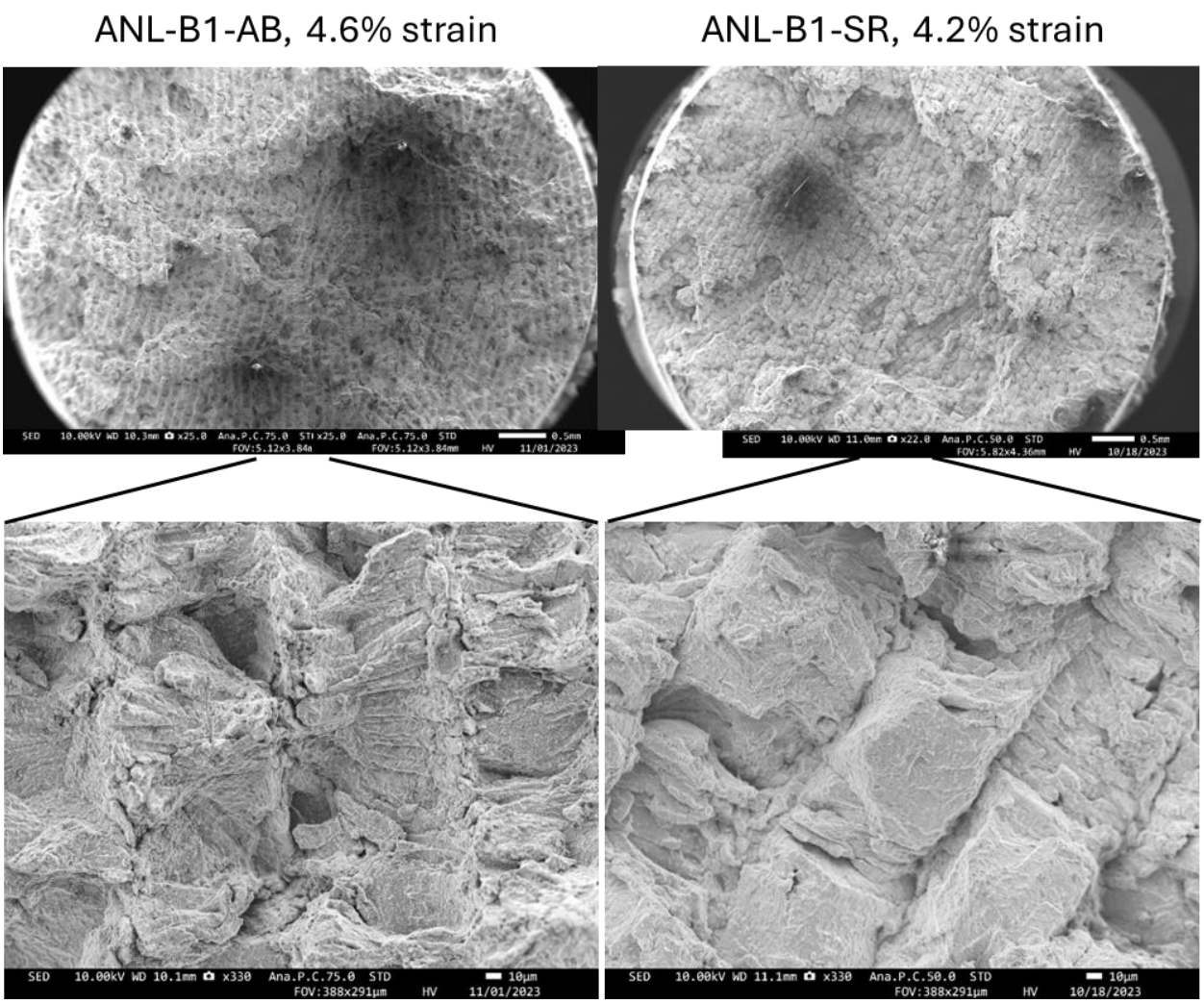

Figure 4.13. Fractographic images of ANL-B1-AB and ANL-B1-SR specimens creep ruptured under 725°C, 100 MPa, in low (top row) and high (bottom row) magnifications.

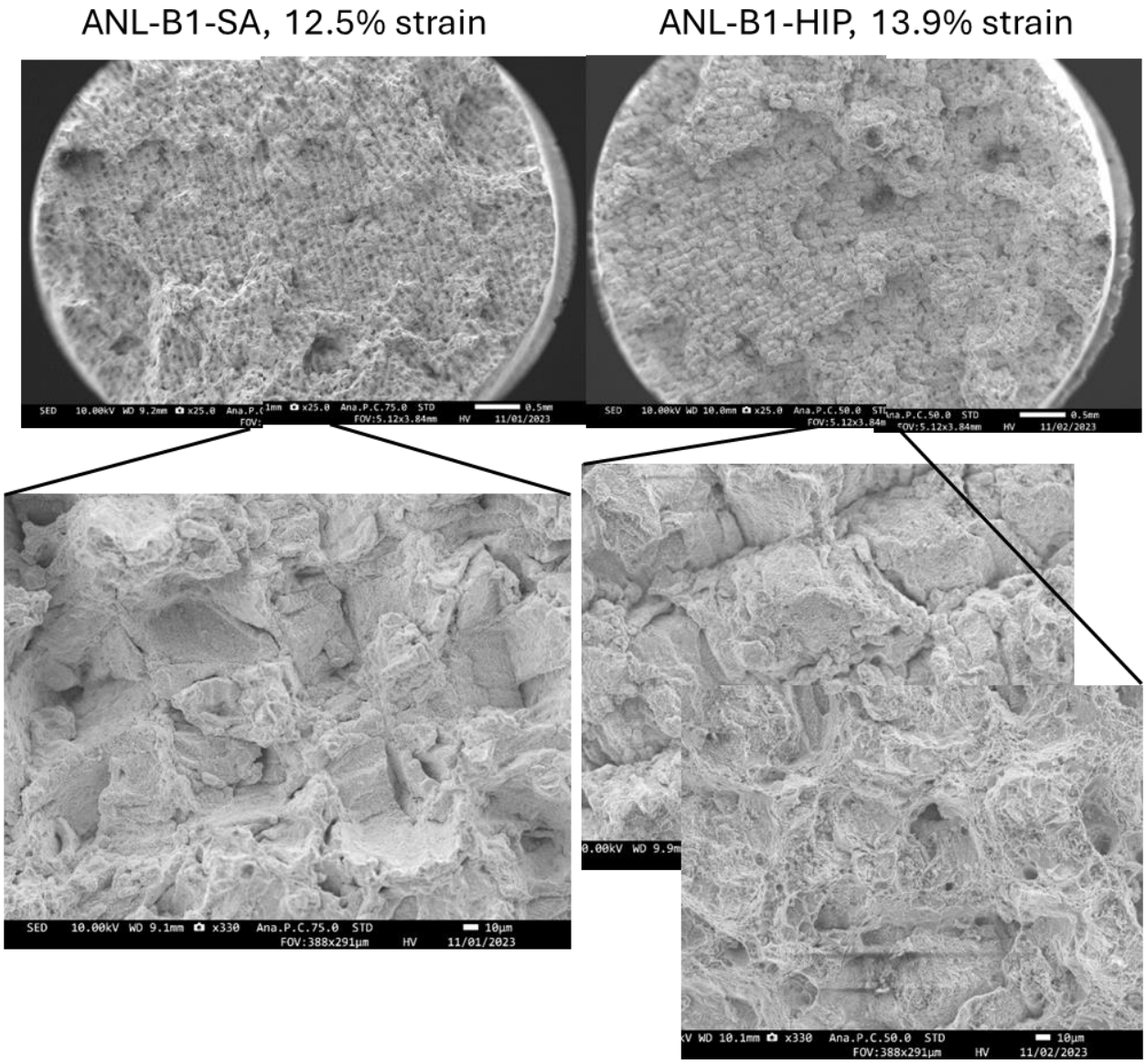

Figure 4.14. Fractographic images of ANL-B1-SA and ANL-B1-HIP specimens creep ruptured under 725°C, 100 MPa, in low (top row) and high (bottom row) magnifications.

While the fractographic images reveal limited differences among the specimens, the precipitates in the materials may provide some clue regarding the differences in creep rupture strains. The SEM radial cross-sectional images are shown in Figure 4.15. The cross-sections are very close to fracture surfaces as illustrated in Figure 4.11. All the samples failed around 650 h, so the thermal annealing effect is similar to all specimens. A prominent feature in ANL-B1-AB and ANL-B1-SR is the large, bright-contrast (in BED mode) precipitates that decorate the grain boundaries. Such a feature is much less noticeable in ANL-B1-SA, and even less noticeable in ANL-B1-HIP. EDS mappings (Figure 4.16 and Figure 4.17) show that the large precipitates have a composition of nominally 52.5Fe-31.1Cr-9.6Mo-4.9Ni-0.95Mn-0.92Si (values in wt.%), in agreement with the composition of the sigma phase found in aged 316 stainless steel [5–7], known to be embrittling. A second phase in bright contrast is much smaller (sub-μm sizes); it exists in all specimens and is enriched

in Mo and Si. It's possible that it is the Laves phase [5]. A third phase is the Cr carbide (likely $M_{23}C_6$, see Section 4.2.2), which has dark contrast in BED mode and is actually more prominent in ANL-B1-SA/HIP than in ANL-B1-AB/SR (C signals more visible for carbides in Figure 4.17 than in Figure 4.16). A fourth phase, not presented in detail in this report, is the Mn-Si-O Rhodonite oxide of tens of nanometers in size. Overall, it is likely that the heavy precipitation of the possible sigma phase on grain boundaries in ANL-B1-AB/SR played a key role in the poor creep ductility in those two specimens. Indeed, as will be shown in Section 4.2.2, the large intermetallic phase serves as the nucleation site of creep voids, and thus embrittling the material.

The reason for the preferred formation of the large embrittling phase in the AB and SR materials requires further studies but is probably related to the chemical segregation at grain boundaries and cell walls, as well as the higher density of preferred nucleation site and faster diffusion path.

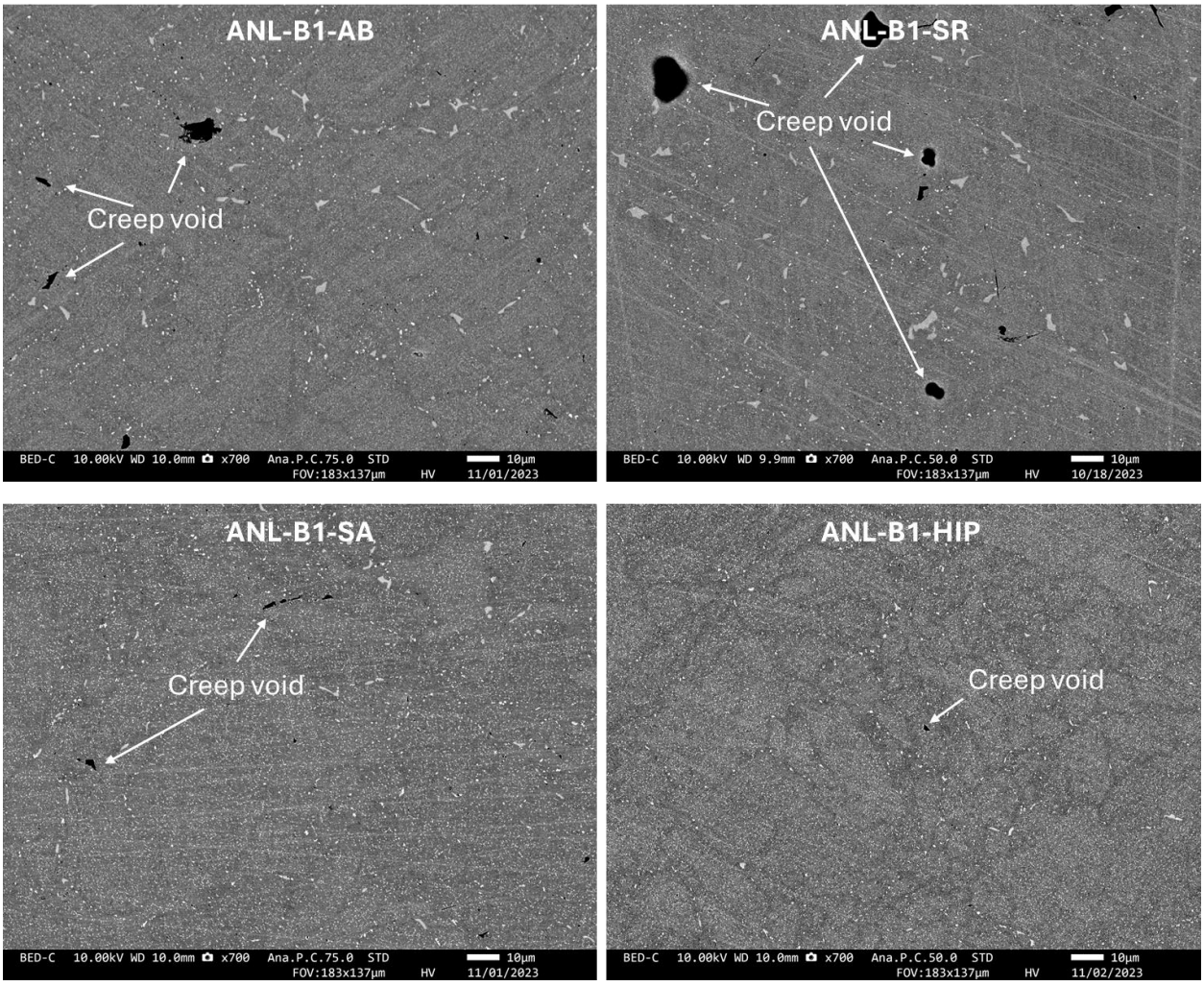

Figure 4.15. SEM-BED images of radial cross-sectional areas near the fracture surfaces of ANL-B1-AB/SR/SA/HIP specimens creep ruptured under 725°C, 100 MPa.

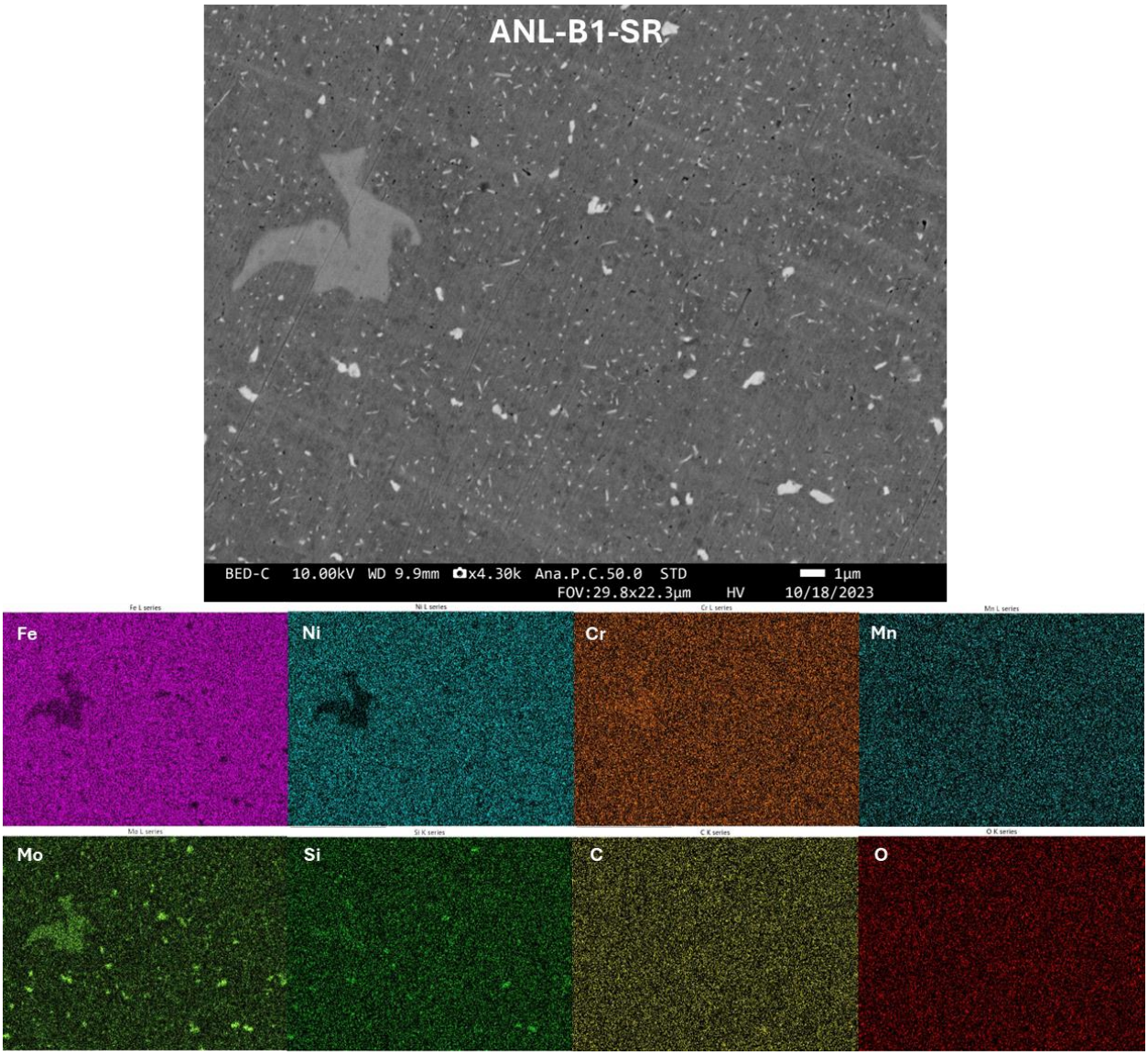

Figure 4.16. An SEM-BED image and corresponding EDS maps of a radial cross-sectional area in the ANL-B1-SR specimen creep ruptured under 725°C, 100 MPa.

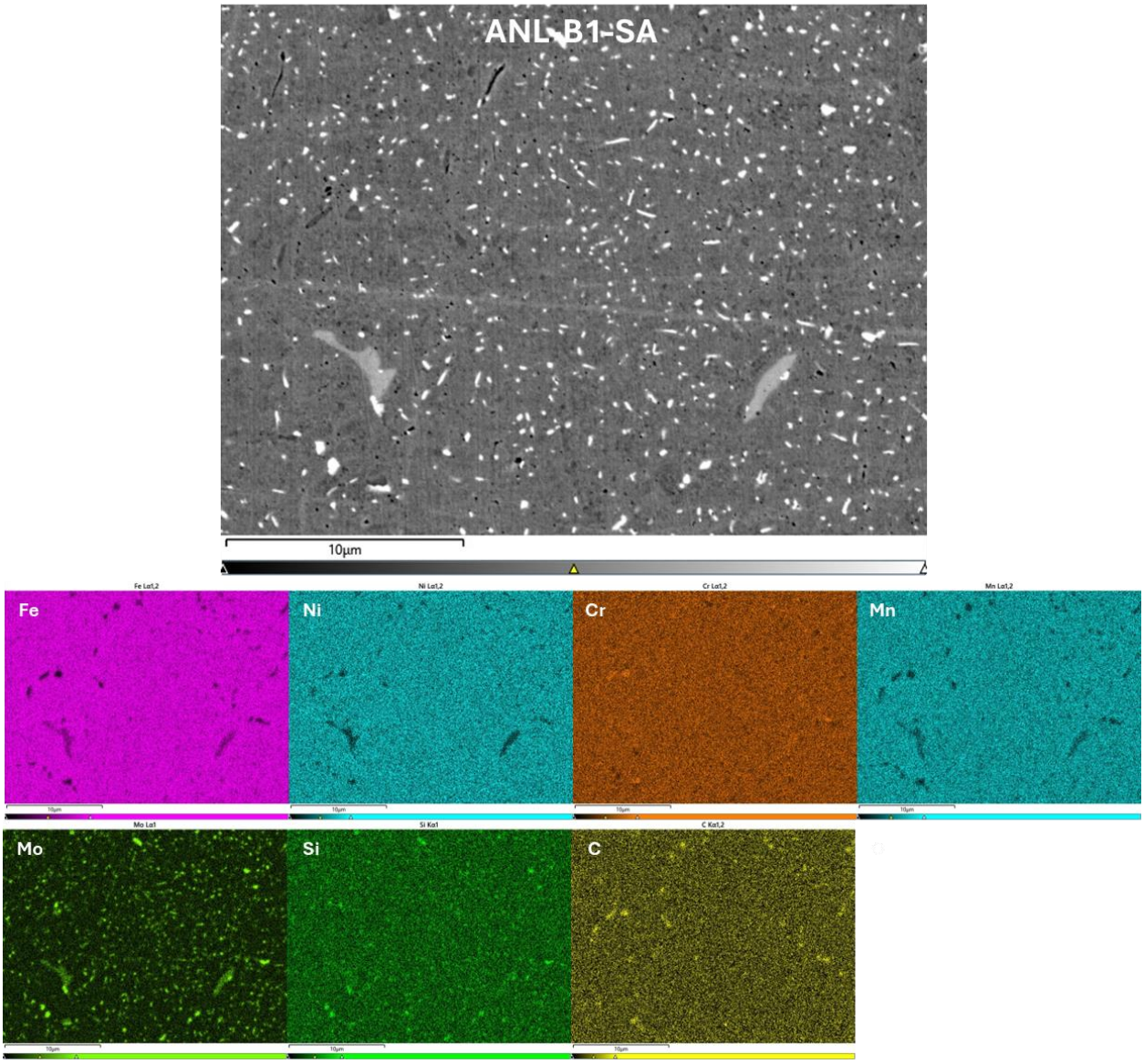

Figure 4.17. An SEM-BED image and corresponding EDS maps of a radial cross-sectional area in the ANL-B1-SA specimen creep ruptured under 725°C, 100 MPa.

4.2.2 Batch variation

Figure 4.18 shows the creep curves of the ANL-B1-SR and ORNL-B1-SR specimens tested under 725°C, 100 MPa. As listed in Table 2.1 and Table 2.2, the two materials were printed using different batches of powders (Prax-AM316H-2 vs. Prax-AM316H-3) on different machines (Renishaw AM400 vs. GE Concept Laser). Their creep behaviors are very different; ORNL-B1-SR outperforms ANL-B1-SR with a lower minimum creep rate, a higher rupture strain, and a much longer rupture life. In this section, microstructural observations will be used to explain the differences in creep damage (Section 4.2.2.1) and in creep deformation (Section 4.2.2.2).

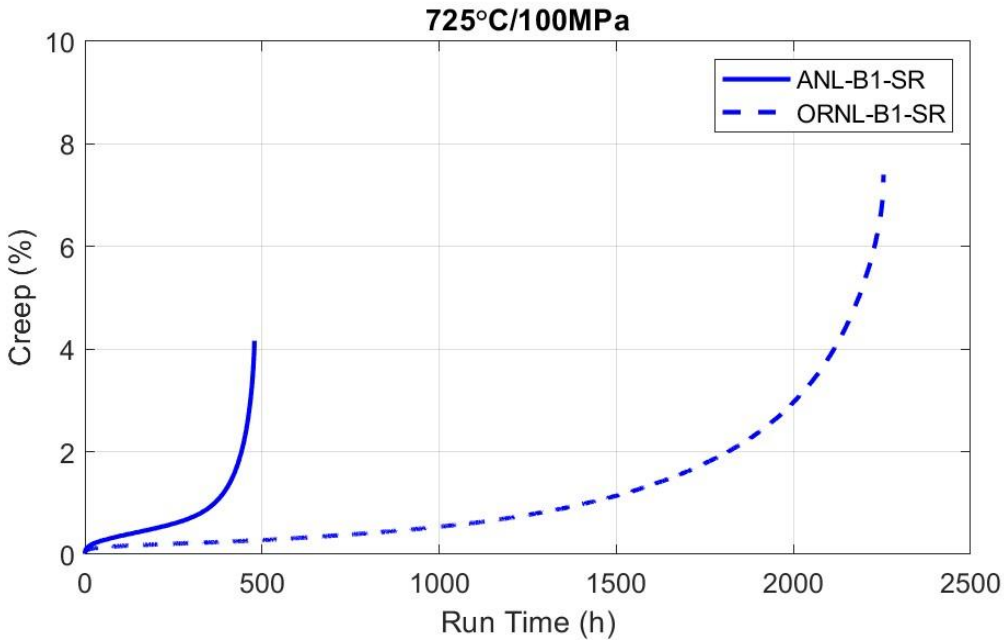

Figure 4.18. Creep curves of the ANL-B1-SR and ORNL-B1-SR specimens tested under 725°C, 100 MPa.

4.2.2.1 Creep damage

The pre-deformation grain structures of ANL-B1-SR and ORNL-B1-SR, as shown in Figure 4.19, are quite different; the ANL grains have the chevron "V" shapes along the build direction with an average size of 40 μm, but the ORNL grains have the elongated columnar shapes with an average size of 81 μm. It is known that a high energy density in the laser printing process promotes the formation of columnar grains. The energy densities of ORNL-B1 and ANL-B1 are 71 kJ/m^3 and 53 kJ/m^3, respectively, agreeing with the observed differences in grain structures.

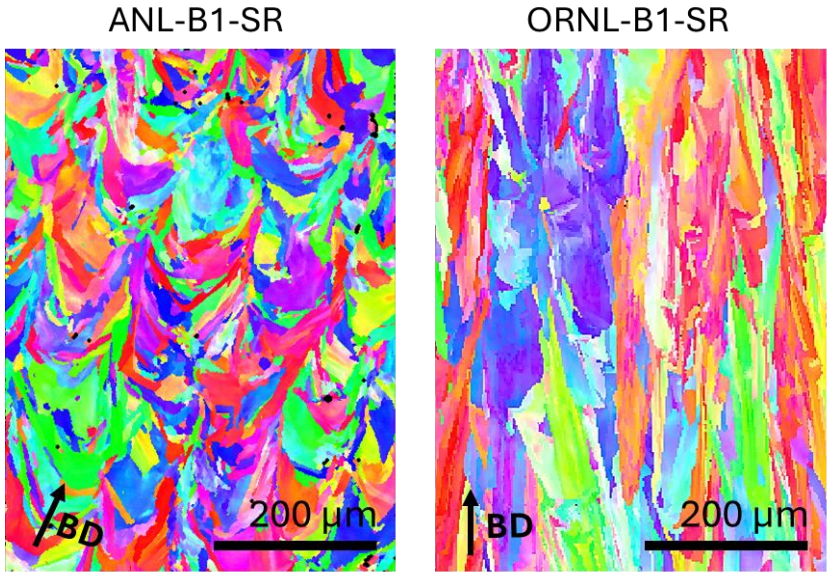

Figure 4.19. EBSD maps showing the pre-deformation grain structures in ANL-B1-SR and ORNL-B1-SR specimens.

After the specimens ruptured under 725°C, 100 MPa creep conditions, SEM, EBSD and EDS were performed to characterize the creep cracks. Figure 4.20 shows the crack morphologies in the axial cross-sections near the fracture surfaces of the two specimens, in SEM-BED imaging mode. It is seen that the population of cracks in ANL-B1-SR is much higher than that in ORNL-B1-SR. The cracks are intergranular (Figure 4.20) and are formed by void coalescence. In areas where individual voids are present, as pointed by the red arrows in Figure 4.20, it is evident that the voids are formed preferably next to the large, bright particles that have been presented in Section 4.2.1 and Figure 4.16, which are likely the sigma phase as discussed in Section 4.2.1.

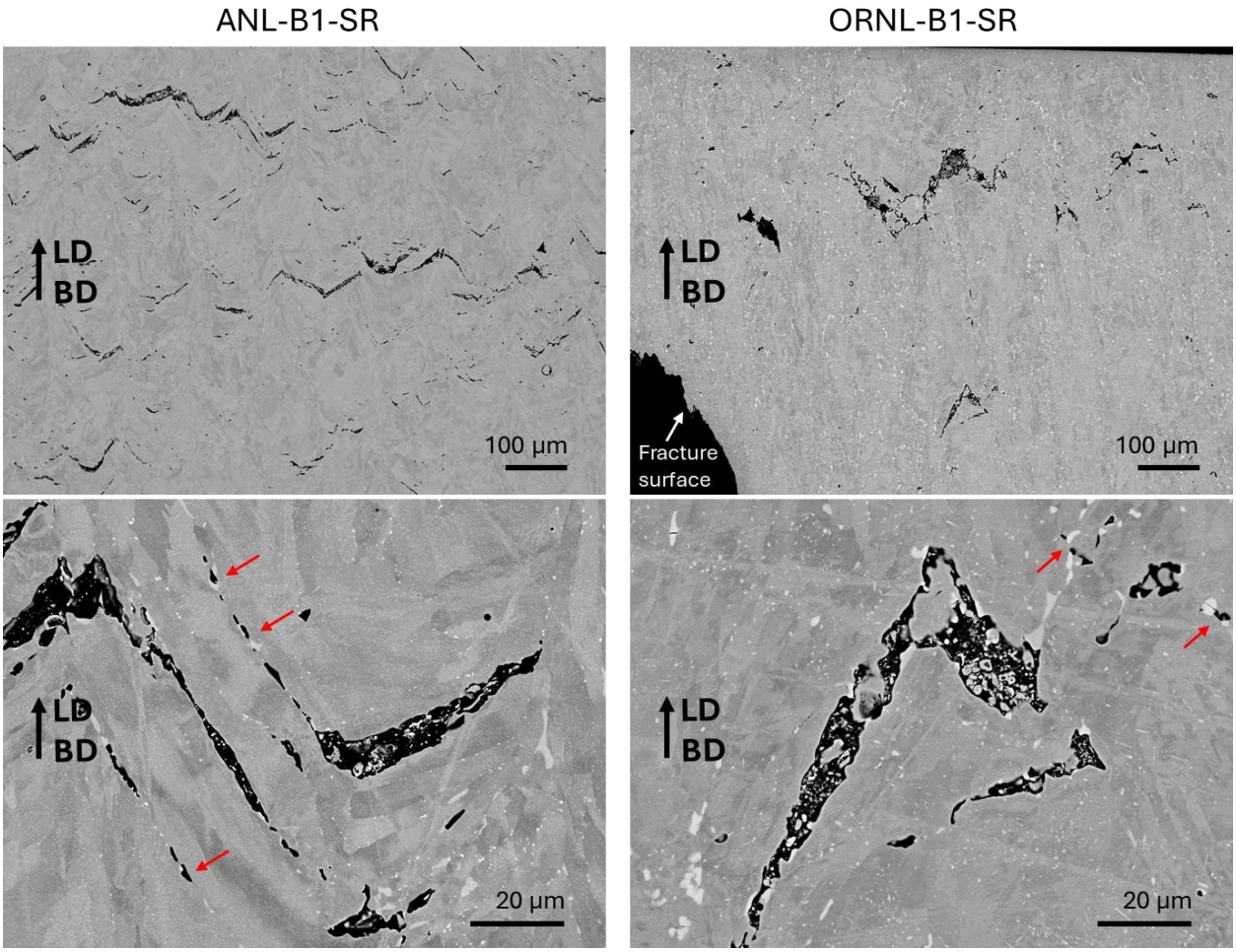

Figure 4.20. Crack morphologies in the axial cross-sections near the fracture surfaces of ANL-B1-SR and ORNL-B1-SR creep tested under 725°C, 100 MPa. Red arrows point to areas that shows creep voids form preferably next to the large, bright particles.

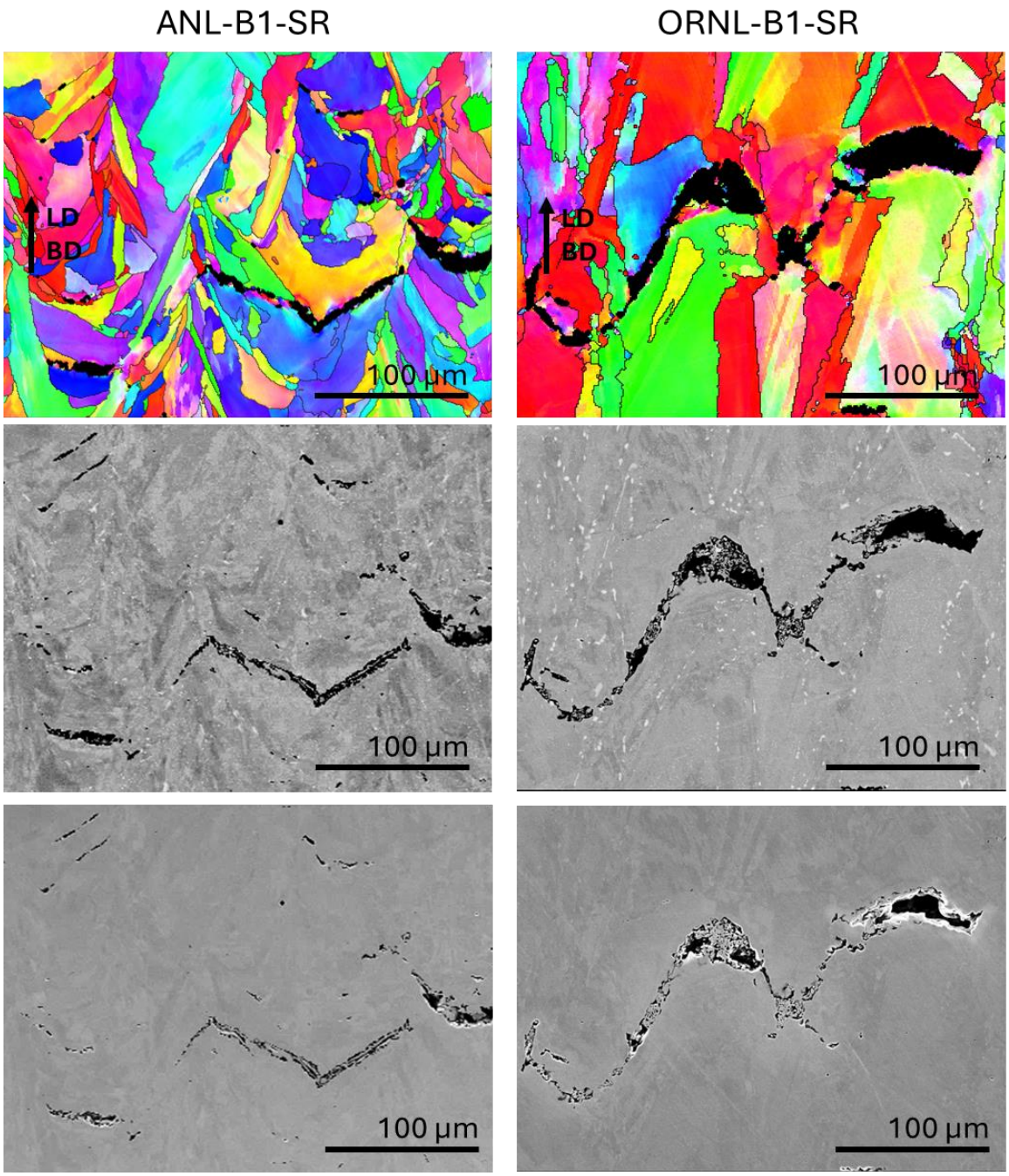

Figure 4.21. EBSD maps (top row), SEM-BED images (middle row) and SEM-SED images (bottom row) showing crack regions in ANL-B1-SR and ORNL-B1-SR creep ruptured under 725°C, 100 MPa.

Looking at Figure 4.19 and Figure 4.20, the lower population of cracks in ORNL-B1-SR can be explained by the larger grain sizes, hence the smaller grain boundary areas, of this material compared to ANL-B1-SR. As the cracks tend to form perpendicularly to the loading direction (LD) (i.e. transverse to the gauge), the elongated columnar grains in ORNL-B1-SR are particularly favorable when the LD is along the longer axes of the grains, which is along the BD. The performance of the materials in the transverse direction may be very different from this vertical direction and will be evaluated in FY 25.

4.2.2.2 Creep deformation

Prior to testing, at the nanoscale, both materials have the dislocation cell walls decorated with round $MnSiO_3$ Rhodonite particles and cuboidal $M_{23}C_6$ precipitates, all being tens of nanometers in size as shown in Figure 4.22. The $MnSiO_3$ Rhodonite particles are formed during the laser printing process, while the $M_{23}C_6$ precipitates are formed during the SR treatment (650°C, 24 h). What varies is the density of the $M_{23}C_6$ precipitates, with ORNL-B1-SR being much higher than ANL-B1-SR. The higher carbon concentration in the Prax-AM316H-3 powder (0.08 wt.%) compared to that in the Prax-AM316H-2 powder (0.06 wt.%) is likely responsible for this difference.

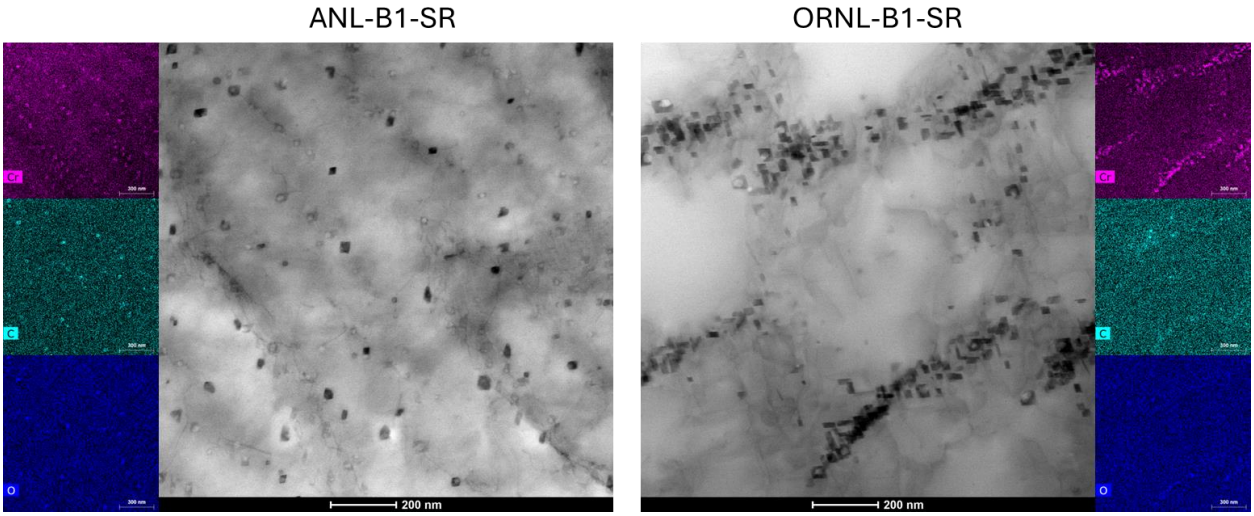

Figure 4.22. STEM bright field images and corresponding EDS maps showing the precipitates on dislocation cell walls in ANL-B1-SR and ORNL-B1-SR materials prior to creep tests.

During creep tests, the precipitate structure continued to evolve. Figure 4.23 and Figure 4.24 show the STEM images and EDS maps of the crept ANL-B1-SR and ORNL-B1-SR materials. Recall that ANL-B1-SR has a rupture time of 479 h and ORNL-B1-SR has 2254 h; it means that the thermal effect is more pronounced in ORNL-B1-SR. In both materials, the dislocation cell structure is preserved during the test, but the cell walls seem much thinner. Similar to the pre-test condition, the post-test materials have secondary phase particles decorating the dislocation cell walls. Those particles act as stabilizers to the cell structure and are the reason that the cell structures are maintained during the tests. The EDS maps in Figure 4.23 and Figure 4.24 show that the cuboidal particles are enriched in Cr, Mn, C and O. Electron diffraction and selected-area darkfield imaging (Figure 4.25) show that they are the $M_{23}C_6$ phase with a lattice constant 3 times that of the austenitic matrix. Compared to the pre-deformation material, the $M_{23}C_6$ precipitates grow larger in the post-deformation material (Figure 4.26) due to the extended aging at the test temperature (725°C).

Besides the $M_{23}C_6$ phase, another phase present at the nanoscale is the rod-like Mo, Si-rich phase. Those particles seem to precipitate on dislocation cell walls or grain boundaries but grow at their preferred crystallographic directions. They could be the Laves phase or molybdenum silicide, to be determined by x-ray or electron diffraction.

The $MnSiO_3$ Rhodonite phase, which is introduced into the materials in the laser printing process, is still present in the creep-tested materials in the form of round, tens-of-nm sized particles on dislocation cell walls.

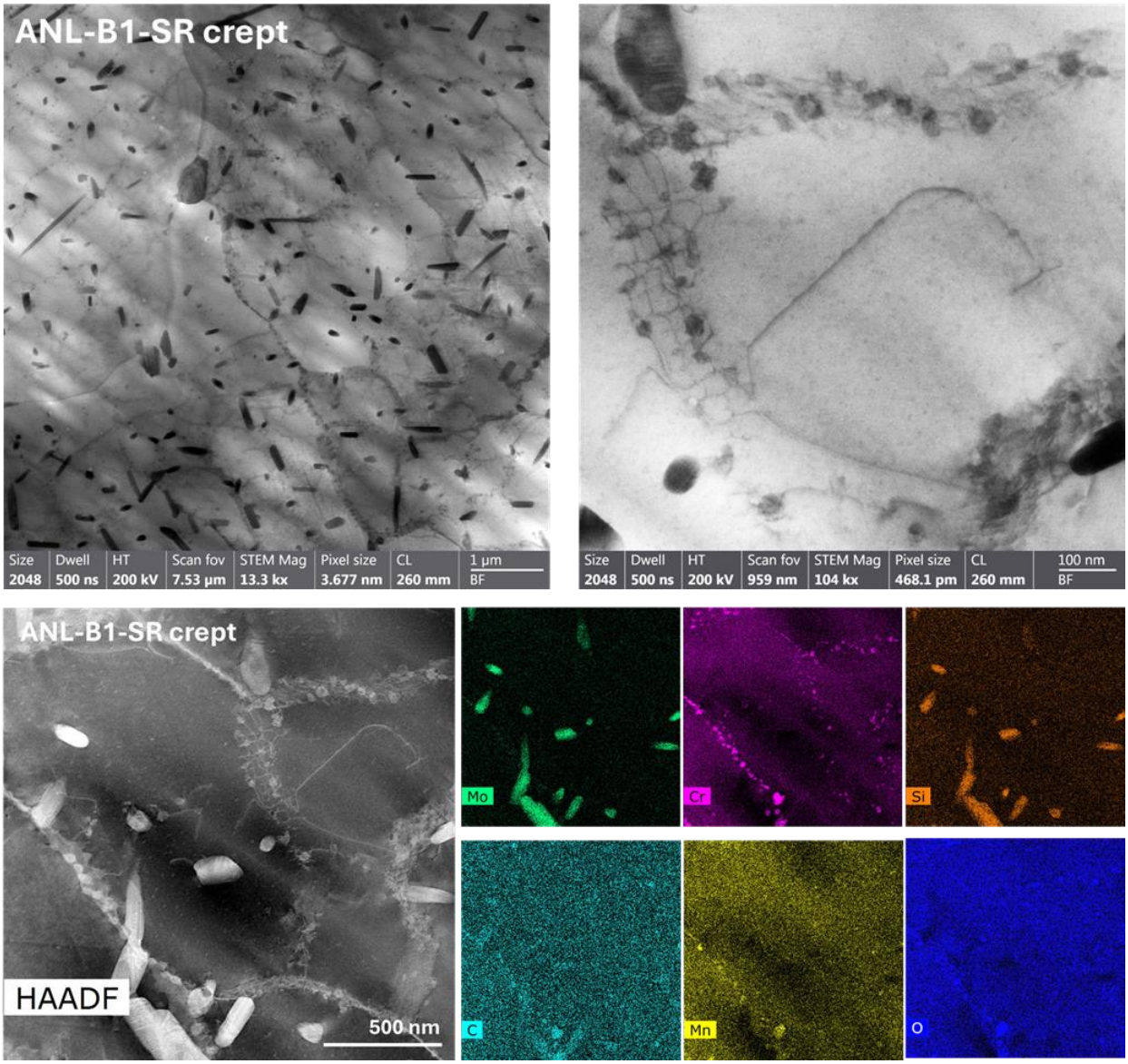

Figure 4.23. STEM bright-field images (top row) and EDS maps (bottom row) of areas in ANL-B1-SR material creep tested under 725°C, 100 MPa.

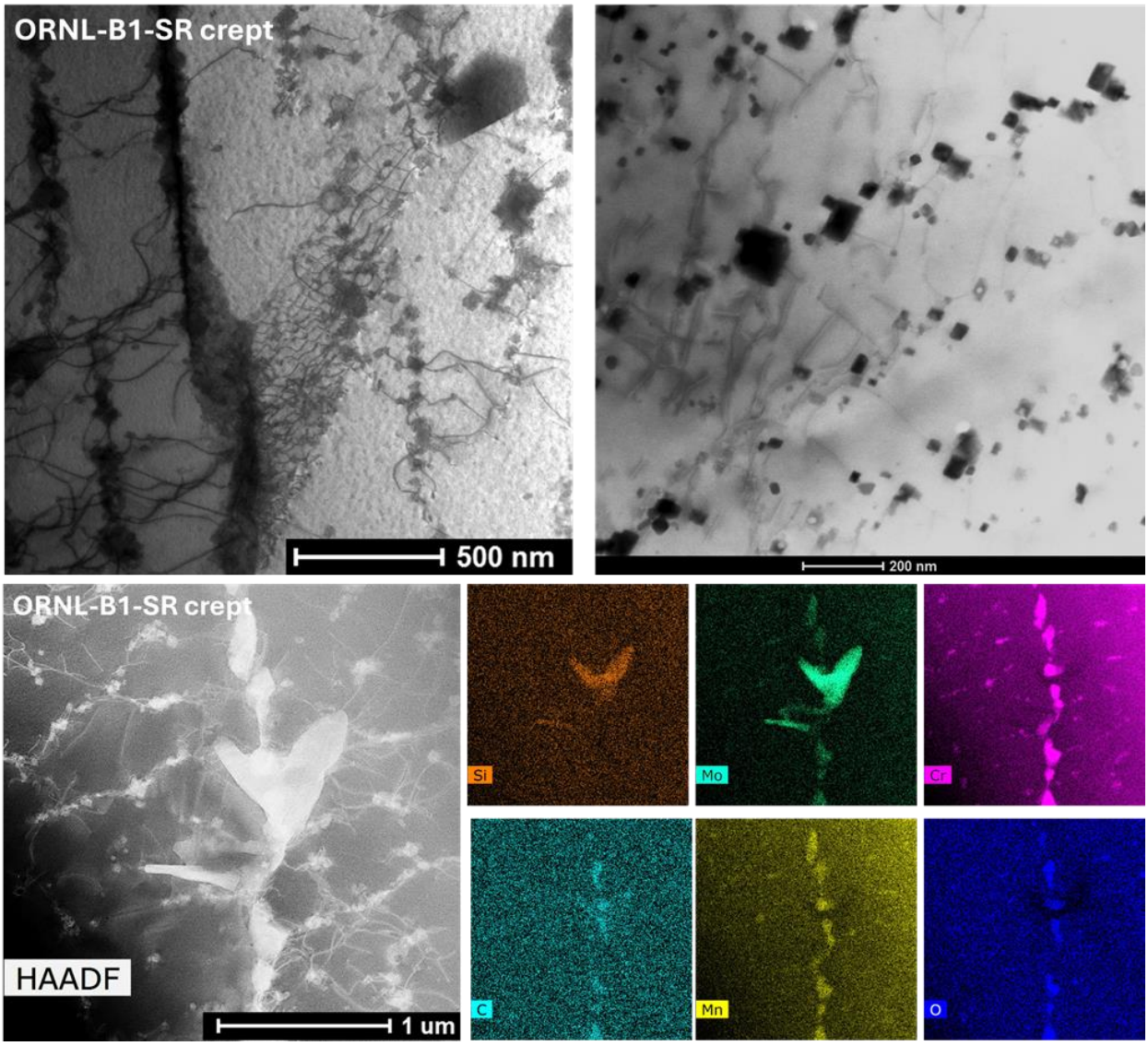

Figure 4.24. STEM bright-field images (top row) and EDS maps (bottom row) of areas in ORNL-B1-SR material creep tested under 725°C, 100 MPa.

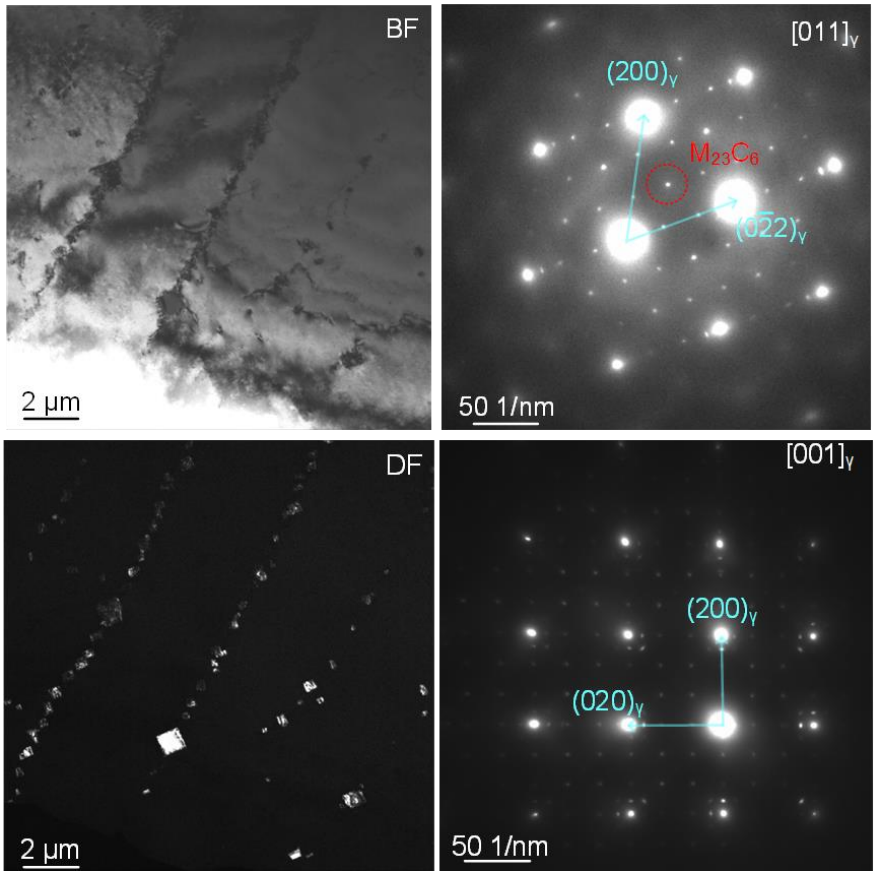

Figure 4.25. Electron diffraction and selected-area darkfield imaging of ORNL-B1-SR creep tested under 725°C, 100 MPa, confirming that the cuboidal precipitates are the $M_{23}C_6$ phase.

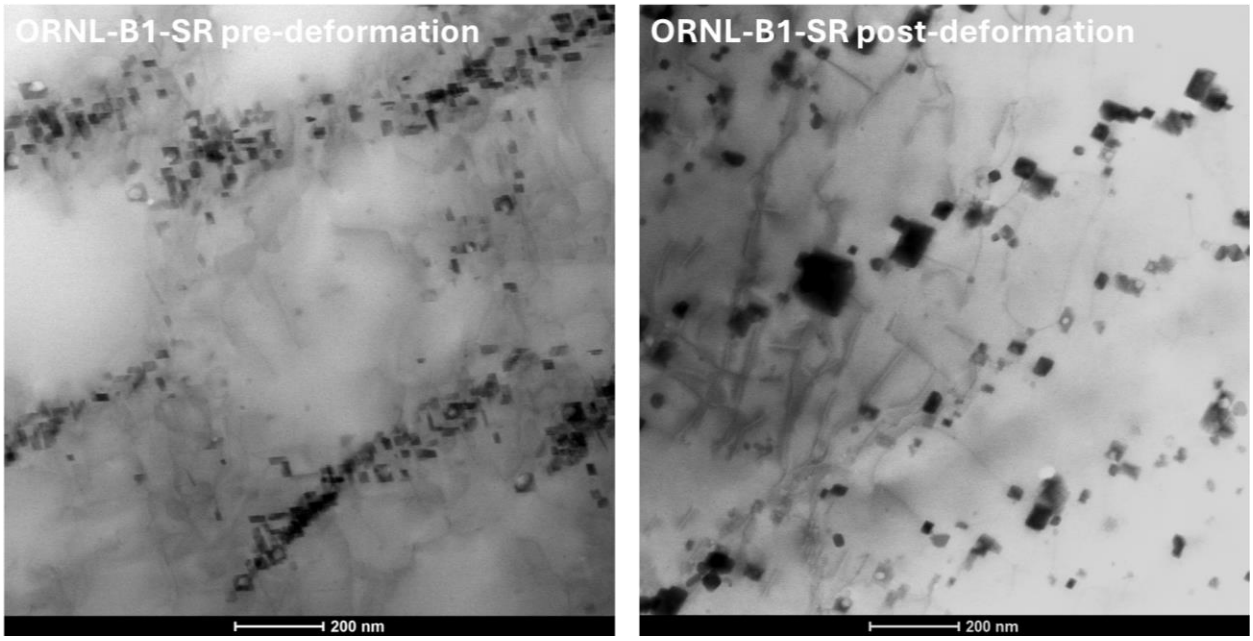

Figure 4.26. Comparison of $M_{23}C_6$ precipitates on dislocation cell walls between the pre- and post-deformation ORNL-B1-SR materials.

From the images presented in this section, it is seen that the ORNL-B1-SR material has a higher density of precipitates compared to ANL-B1-SR. This provides an explanation to the lower minimum creep rate in this material. We consider the effect of precipitates on the creep behavior of the material in the form of a friction stress, $\Delta\sigma_p$ (p for precipitate), due to the retardation of dislocation motion by those precipitates. $\Delta\sigma_p$ of ORNL-B1-SR is expected to be substantially larger than $\Delta\sigma_p$ of ANL-B1-SR. The effective stress, σ_{eff}, applied to the material during the creep test can be expressed as:

$$\sigma_{\text{eff}} = \sigma_{\text{appl}} - \Delta\sigma_{\text{p}} - \Delta\sigma_{\text{d\_th}},$$

where σ_{appl} is the applied stress and $\Delta\sigma_{\text{d\_th}}$ is a friction stress from dislocations. σ_{eff} of ORNL-B1-SR is expected to be smaller than σ_{eff} of ANL-B1-SR due to the higher precipitate density. The minimum creep rate can be expressed by [8]:

$$\dot{\varepsilon}_{\text{m}} = A\frac{DGb}{kT}\left(\frac{\sigma_{\text{eff}}}{G}\right)^n,$$

where A is a constant, D is the diffusion coefficient, k is the Boltzmann constant, T is the absolute temperature, and n is the stress exponent. The smaller σ_{eff} in ORNL-B1-SR results in a smaller $\dot{\varepsilon}_{\text{m}}$, explaining the experimental observation. The quantification of this effect will be performed in a continued study.

4.3 Summary of creep study on LPBF 316H SS

A summary of FY24's creep testing work on LPBF 316H SS is provided below:

- A total of 34 rupture tests were completed under 600°C/240 MPa, 725°C/100 MPa, and 800°C/53.3 MPa, with rupture times ranging from 69 to 2254 h.
- The rupture times of most tests fall within the scatter band of wrought 316H SS.
- The rupture strains of the LPBF materials tend to decrease with increasing temperature and are in general lower than the wrought counterpart. The rupture strains of AB & SR materials are in general lower than 10% while those of SA & HIP materials are higher than 10% when tested at 725°C and above. The heavier precipitation of large, embrittling Mo, Cr, Si-rich particles along grain boundaries in AB & SR materials compared to that in SA & HIP materials may explain the difference in rupture strains.
- The powder chemistry has an impact on the creep performance; a higher carbon concentration and a lower silicon concentration might be favorable.
- A higher porosity reduces the rupture strain; its impact on other creep properties requires further evaluation.
- The grain structure is likely a key factor in the creep damage stage. Elongated columnar grains have fewer cracks than Chevron V-shaped grains when loaded along BD, likely leading to longer rupture times and higher rupture strains.
- A high density of nanoscale precipitates lowers the minimum creep rate, which can be explained by imposing a friction stress during creep deformation.

5 Fatigue/creep-fatigue tests

5.1 Test results

Fatigue and creep-fatigue tests were performed on three AM builds at two laboratories. Samples with and without post-build heat treatments were included in this study. All cyclic tests were fully reversed, strain-controlled tests, and were performed with a nominal strain amplitude of 0.5% and a strain rate of 0.1%/s. All testing was performed on specimens with a machined and polished gauge surface. The test results are summarized in Table 5.1. Note that the cyclic lives were defined differently between the two laboratories: ANL used a 25% load drop, while INL used a 20% load drop. Nonetheless, the differences in cyclic life between these two definitions were negligibly small due to the rapid load change at the end of the cyclic test.

Figure 5.1 shows an example of fatigue test performed on a SR specimen obtained from AM build ANL-B1. The specimen's strain was cycled between ±0.5% while the stress response was continuously recorded during the test. A brief period of cyclic hardening (less than 20 cycles) was observed in this sample, followed by an extended phase of cyclic softening. As expected, the hysteresis loop evolved slowly during the test as shown in Figure 5.1 (c). The final failure occurred abruptly at around 900 cycles.

Table 5.1. Fatigue and creep-fatigue test results on AM 316H SS

AM build	Sample ID	Heat treatment [1]	Test temperature (°C)	Strain AMP (%)	Hold time (min)	Cyclic life [2] (cycles)
ANL-B1	51-1-F3	AB	550	0.51	-	775
	51-2-F3	SA	550	0.51	-	356
	51-3-F3	SR	550	0.50	-	896
	51-4-F3	HIP	550	0.50	-	1062
	51-1-F2	AB	550	0.52	6	403
	51-2-F2	SA	550	0.52	6	330
	51-3-F2	SR	550	0.50	6	742
	51-4-F2	HIP	550	0.50	6	720
ORNL-B1	B1P7B-2	SR	550	0.52	6	2350
	B1P8B-1	SA	550	0.51	6	2225
	B1P9B-1	HIP	550	0.52	6	1481
LANL-B2	LCF-1	SR	550	0.5	30	567
	LCF-2	SR	550	0.5	6	2037
	LCF-6	SA	550	0.5	6	1037
	LCF-7	SA	550	0.5	-	2191
	LCF-4	SR	650	0.5	-	1313
	LCF-3	SR	650	0.5	30	302
	LCF-9	SA	650	0.5	-	1070 [3]
	LCF-8	SA	650	0.5	30	168

[1] As Built = AB, Solution Annealed = SA, Stress Relieved =SR, and Hot Isostatic Pressed = HIP

[2] For the tests conducted on ANL-B1 and ORNL-B1, failure lives were recorded at 25% load drop. For the tests on the AM build LANL-B2, failure lives were recorded at 20% load drop.

[3] Cracking occurred outside of the extensometer gauge.

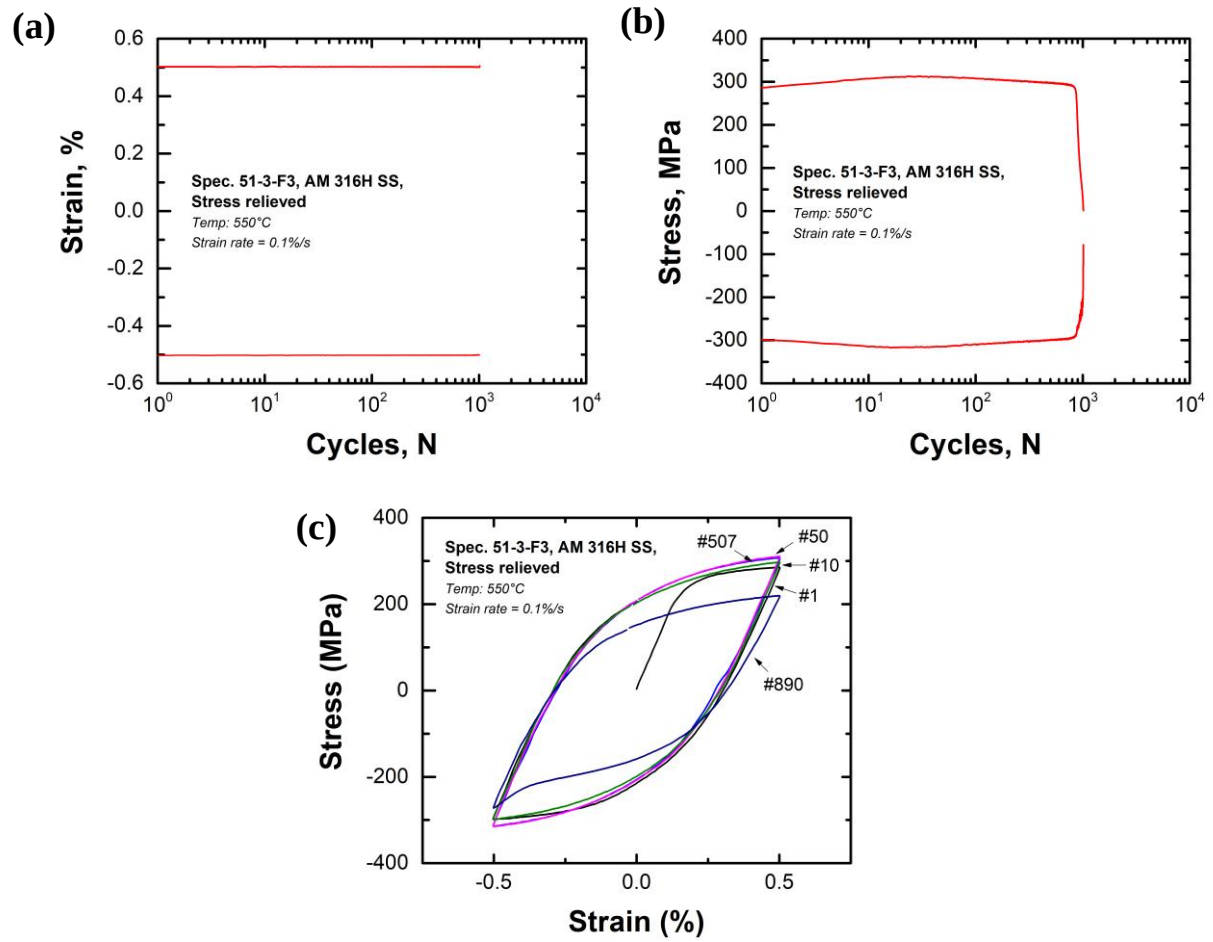

Figure 5.1. A fatigue test on a SR sample extracted from ANL-B1. The strain (a) and stress (b) profiles, and selected hysteresis loops (c) during the test.

Similarly, creep-fatigue tests were performed under a constant strain amplitude of 0.5% with a strain rate of 0.1%/s. For each cycle, the strain was held at its maximum for 6 or 30 minutes to induce creep deformation. As an example, Figure 5.2 shows the creep-fatigue test performed on an ANL-B1-HIP specimen. In this test, the specimen experienced cyclic hardening for a much longer duration (~250 cycles), while the subsequent steady-state and softening phases were relatively short. The 6-min hold at the maximum strain resulted in varying levels of stress relaxation, ranging from 30 to 50 MPa, as shown in Figure 5.2 (c). The final failure of this sample occurred at about 730 cycles.

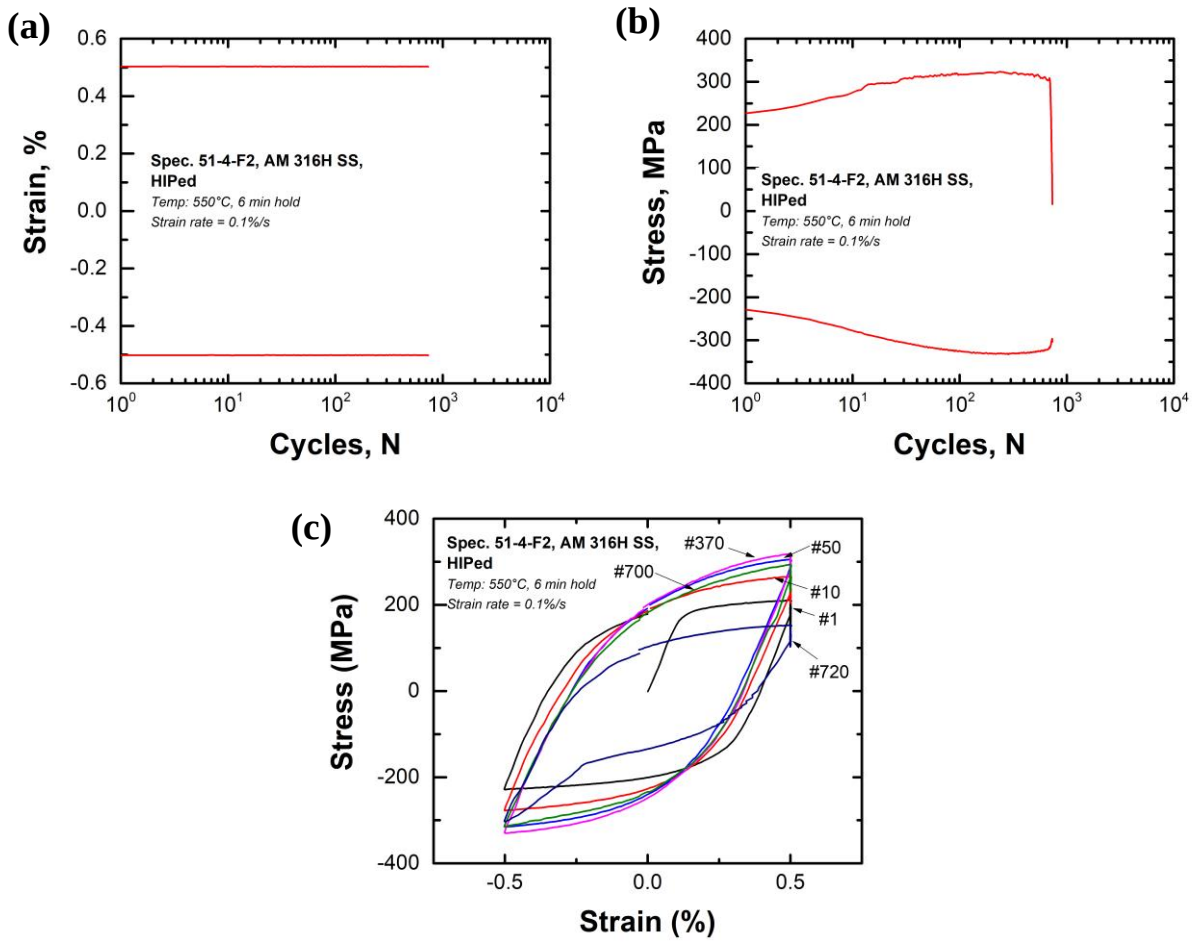

Figure 5.2. A creep-fatigue test on a HIP sample extracted from ANL-B1. The strain (a) and stress (b) profiles, and selected hysteresis loops (c) during the test.

The fatigue and creep-fatigue test results obtained to date are summarized in Figure 5.3. Different heat treatments are represented with different colors in the figure. For all heat treatments, the cyclic lives of creep-fatigue tests were significantly lower than those of fatigue lives. Holding strain at its maximum for 6 min reduced the cyclic lives of AM 316H SS by 10-50% at 550°C. As temperature and hold time increase, the effect of holding becomes more pronounced. At 650°C, the measured cyclic lives with a 30-min hold were approximately 80% lower than those without a hold.

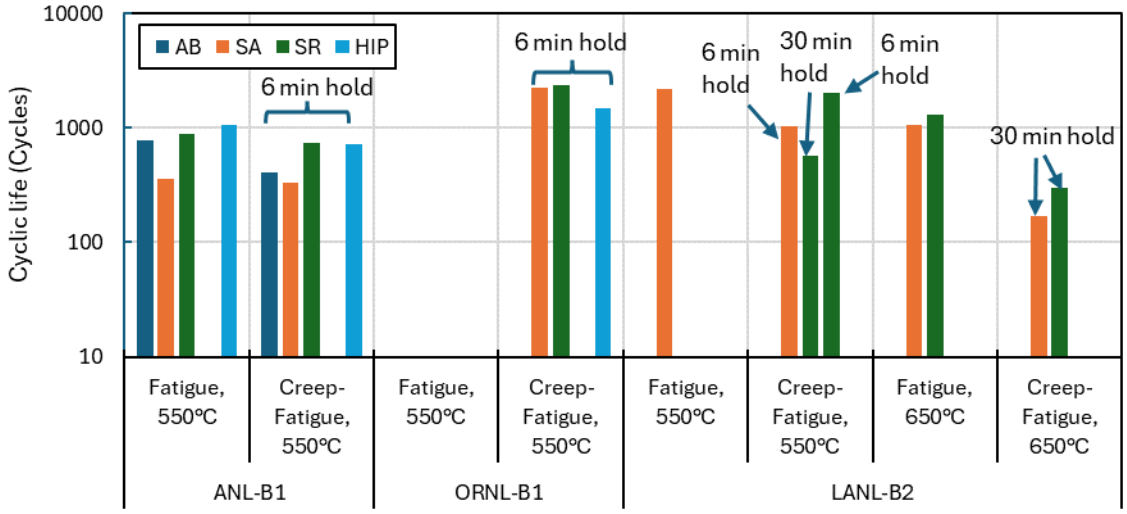

Figure 5.3. Cyclic lives of three AM 316H builds with different post-build heat treatments. Note that the numbers of cycles at 25% load drops were used for ANL-B1 and ORNL-B1, while the numbers of cycles at 20% load drops were used for LANL-B2.

As a cyclic test progresses, the stress response becomes steady over time. As a result, the hysteresis loop remains stable for an extended period. Figure 5.4 shows the hysteresis loops at the midlife cycles of the 550°C tests performed in this study. Note that the five fatigue tests without tensile holding are plotted in Figure 5.4a, and the creep-fatigue tests for different AM builds are plotted in three separate figures. For the AM build ANL-B1, flow-stress serrations can be observed on the hysteresis loops for the AB and SA samples. This instability in cyclic stress may be attributed to dynamic strain aging (DSA), a common phenomenon in austenitic stainless steels deformed at elevated temperatures. In contrast, the hysteresis loops for the SR and HIP samples appear smooth. Both fatigue and creep-fatigue tests exhibit similar observations: DSA is active in the AB and SA samples but is absent in the SR and HIP samples.

For the ORNL-B1 build, gentle stress serrations appear for all SR, SA and HIP samples. Comparing the SA samples of ANL-B1 and ORNL-B1, a sharp contrast is observed: cyclic instability seems suppressed in the ORNL-B1 sample but evident in the ANL-B1 sample. For the LANL-B2 build, all hysteresis loops obtained at 550°C are smooth (Figure 5.4d), including the one tested without holding (see Figure 5.4a). However, at 650°C, both the SR and SA samples of LANL-B2 show the effects of DSA regardless holding time (Figure 5.5). Evidently, the three AM builds examined in this study exhibit different sensitivity to DSA, which may contribute to their cyclic performance at elevated temperatures.

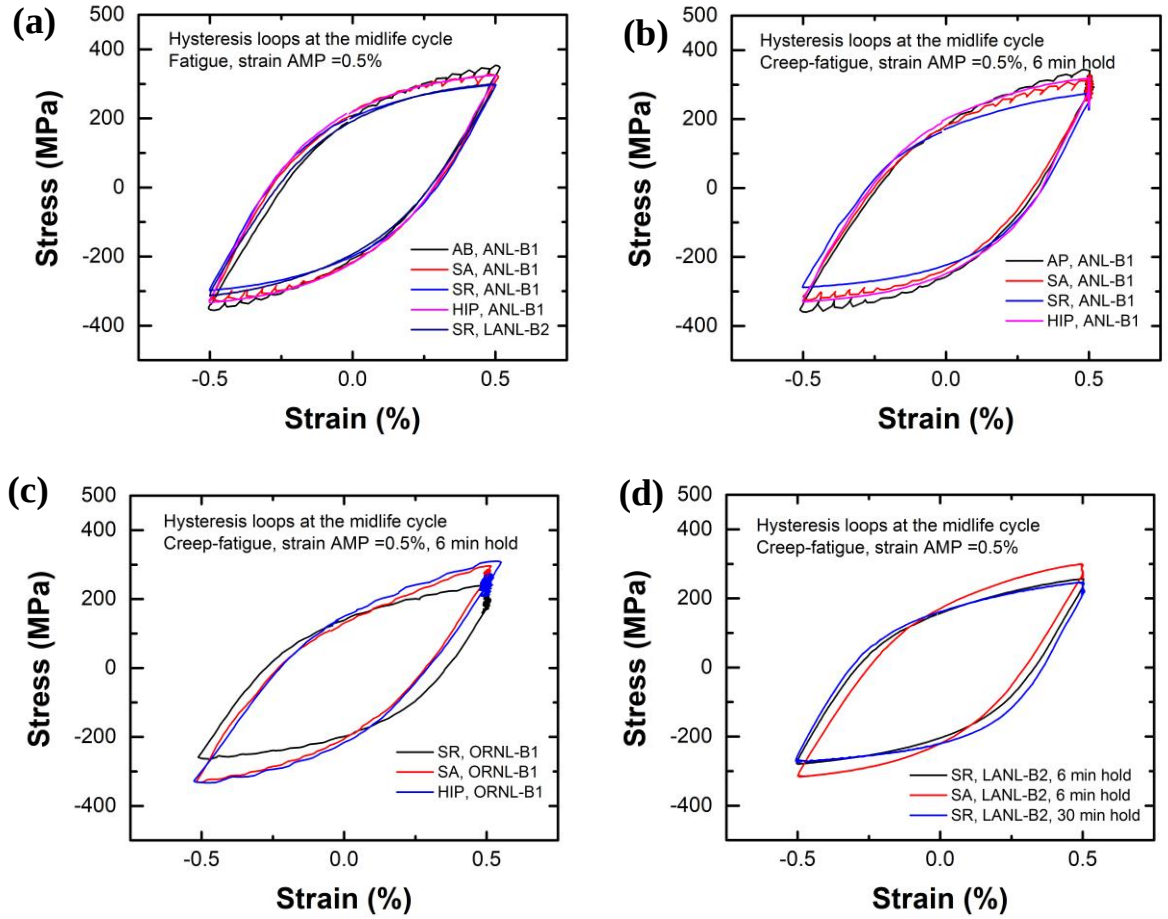

Figure 5.4. The midlife hysteresis loops at 550°C for three AM builds with different post-build heat treatments. Fatigue tests (a), and creep-fatigue tests for ANL-B1 (b), ORNL-B1 (c), and LANL-B2 (d).

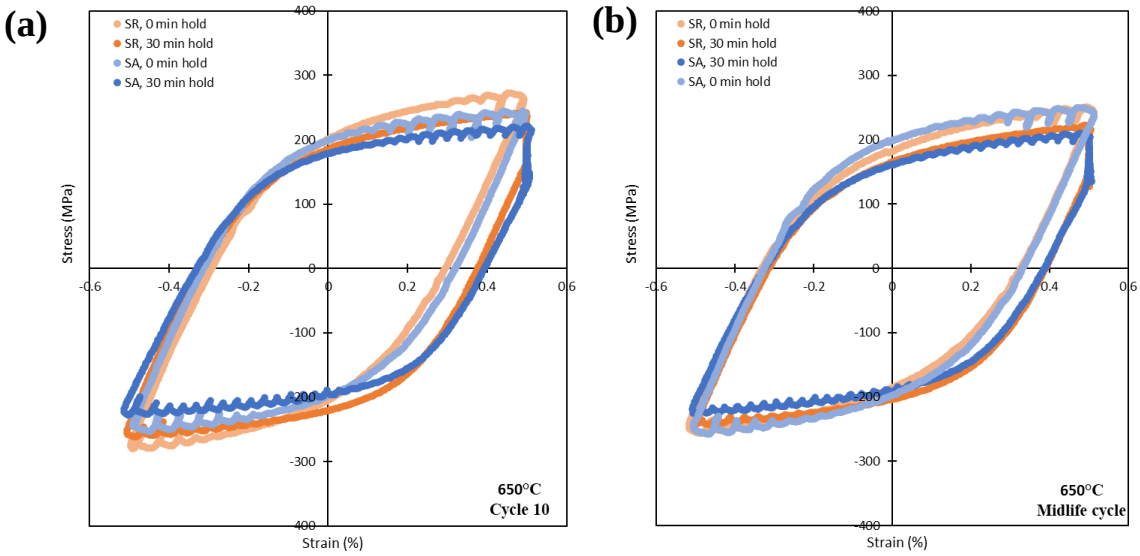

Figure 5.5. Hysteresis loops of the LANL-B2 samples tested at 650 °C for (a) cycle 10 and (b) the midlife cycle.

5.2 Metallographic characterization

After completion of the cyclic tests, the fatigue and creep-fatigue specimens from the LANL-B2 specimens were cross sectioned such that the major crack was bisected, and microscopy could be performed. The cross sections were mounted in epoxy and the metal surface was etched with oxalic acid for 45 seconds. The cross sections for the fatigue specimens are shown in Figure 5.6 to Figure 5.8, and the creep-fatigue in Figure 5.9 to Figure 5.12. In all figures, the loading direction is vertical. Note that Figure 5.8 shows half of the fractured LCF-9 specimen, as this specimen ruptured due to the primary crack occurring outside of the extensometer.

The difference between the SR (Figure 5.7, Figure 5.9 and Figure 5.11) and SA (Figure 5.6, Figure 5.8, Figure 5.10 and Figure 5.12) is clear in the results of the etching. The etching of the SA specimens cleanly revealed the grain boundaries, whereas the etchant attacked not just the grain boundaries, but also portions of the grains in the SR specimens, making the micrographs more difficult to interpret. This is likely due to the high density of dislocations present in the stress relieved condition.

Fatigue cracks, as expected, appear to be fully transgranular. Creep-fatigue cracking has a mixture of trans- and intergranular cracking. This is more clearly seen in the creep-fatigue testing of the solution annealed material (Figure 5.10 and Figure 5.12). In all creep-fatigue specimens, intergranular cracking, due to creep damage and often in segments of a single grain boundary, is visible away from the main crack. Other than the difference in how the etchants affected the surface, there does not appear to be a significant difference between the fracture path of the SR vs. SA materials. It is useful for creep-fatigue testing to determine the degree of intergranular cracking vs. transgranular cracking, to understand the role of creep damage (occurring on the grain boundary) vs. fatigue damage (transgranular). However, this comparison is challenging between SR and SA due to the difficulty in seeing the grain boundaries clearly in the etched SR material. This comparison will require electron microscopy and can be performed in future work.

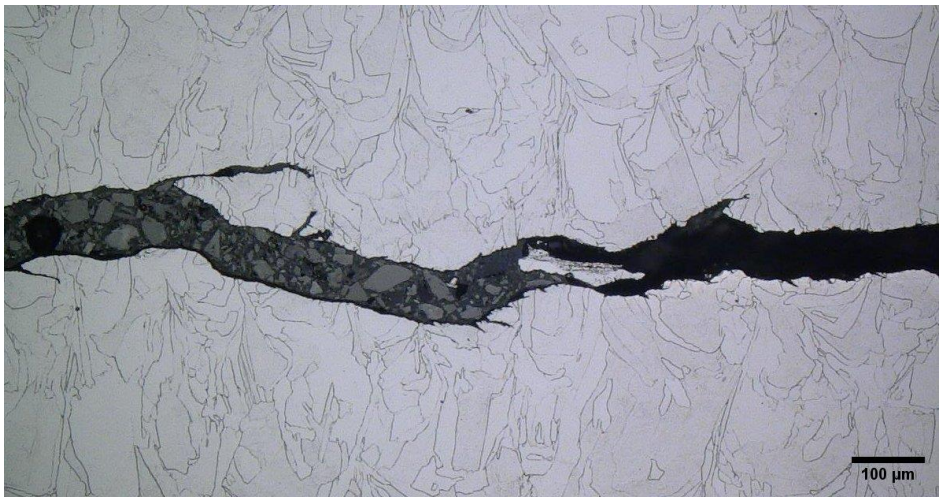

Figure 5.6. Cross section of crack in SA specimen LCF-7, fatigue tested at 550 °C with a Δε of 1%.

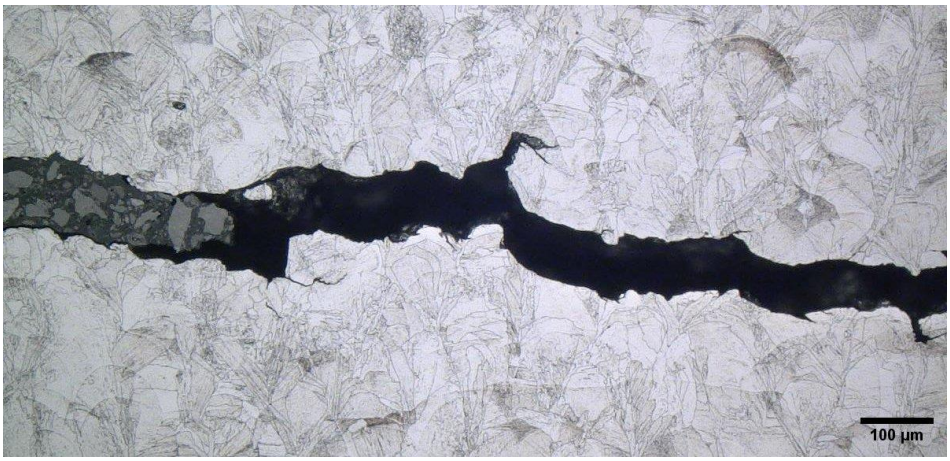

Figure 5.7. Cross section of crack in SR specimen LCF-4, fatigue tested at 650 °C with a Δε of 1%.

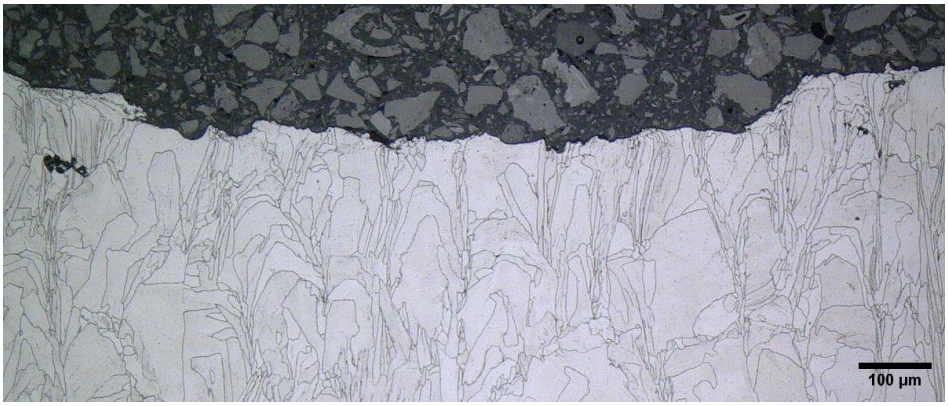

Figure 5.8. Cross section of crack in SA specimen LCF-9, fatigue tested at 650 °C with a Δε of 1%.

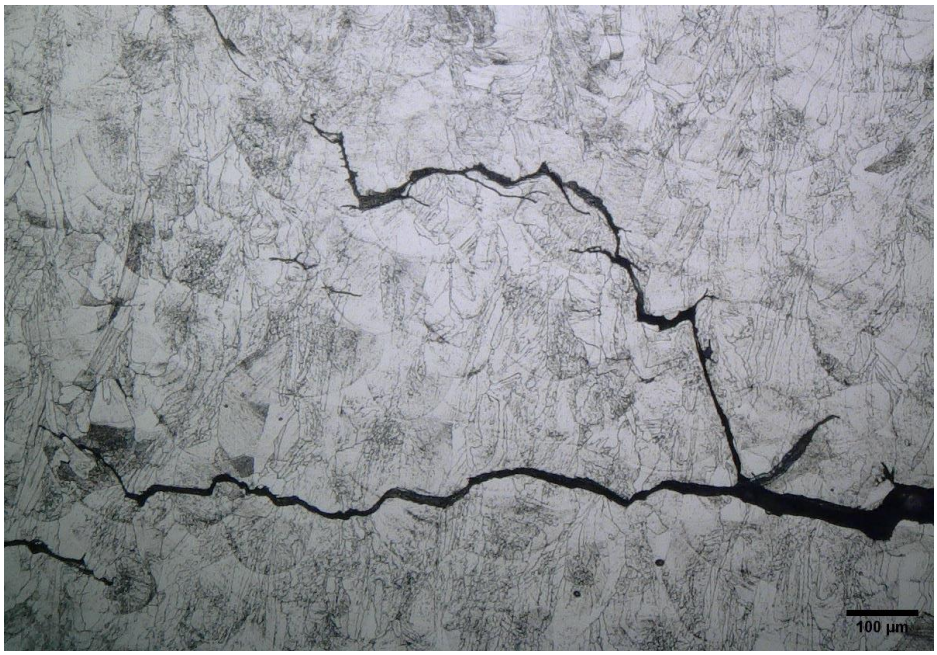

Figure 5.9. Cross section of crack in SR specimen LCF-1, creep-fatigue tested at 550 °C with a Δε of 1% and a hold time of 30 minutes.

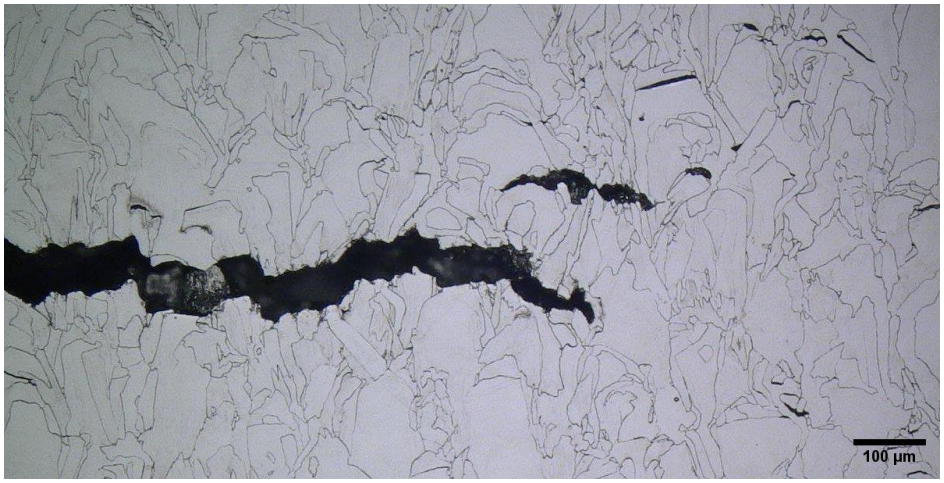

Figure 5.10. Cross section of crack in SA specimen LCF-6, creep-fatigue tested at 550 °C with a Δε of 1% and a hold time of 6 minutes.

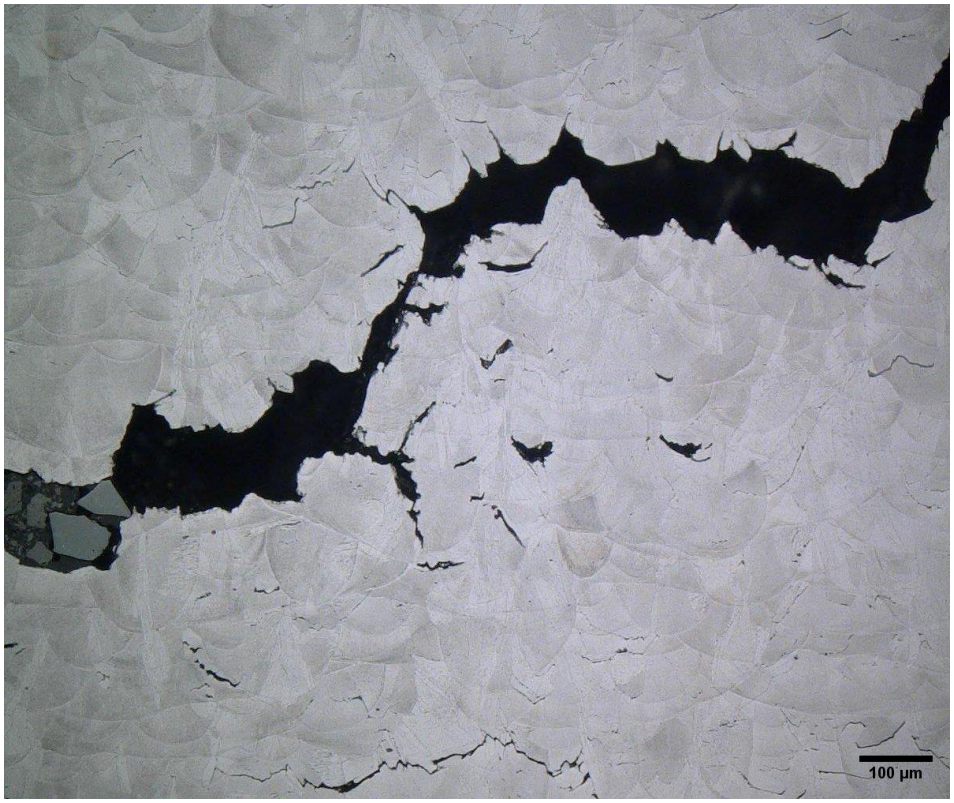

Figure 5.11. Cross section of crack in SR specimen LCF-3, creep-fatigue tested at 650 °C with a Δε of 1% and a hold time of 30 minutes.

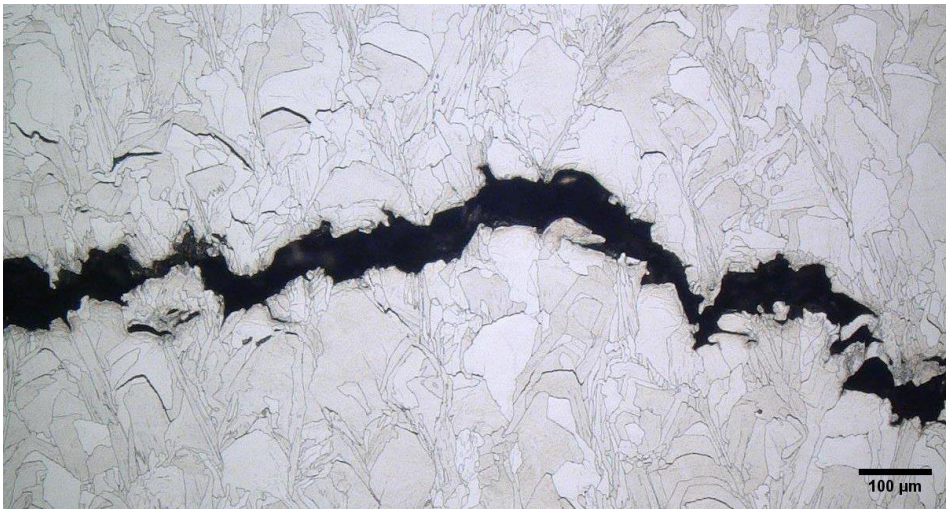

Figure 5.12. Cross section of crack in SA specimen LCF-8, creep-fatigue tested at 650 °C with a Δε of 1% and a hold time of 30 minutes.

5.3 Discussion

Figure 5.13 shows the stress-amplitude profiles for the fatigue and creep-fatigue tests performed at 550°C on different AM builds. For the fatigue tests on SA samples without holding (Figure 5.13a), the initial strength of ANL-B1 was about 20 MPa higher than that of LANL-B2, but similar cyclic hardening behavior was observed for both AM builds. The difference in stress response remained consistent throughout the tests, leading to a higher maximum stress and a shorter fatigue life for the ANL-B1 build. It appears that despite the same post-build heat treatment (SA), differences resulting from the printing process can still influence the fatigue performance of AM materials.

Similar cyclic responses can be seen for the SA treated samples in the creep-fatigue tests with a 6-min hold at each tensile maximum (Figure 5.13b). Once again, similar cyclic hardening behavior was observed for all AM builds. The main difference among them was their initial stress states at the beginning of the cyclic tests. While the initial strength of LANL-B2 and ORNL-B1 were similar, the initial strength of ANL-B1 was much higher. With similar cyclic hardening rates, the maximum stress achieved in the LANL-B2 sample remained lower than that of the ANL-B1 sample, leading to a moderate increase in cyclic life. The difference in cyclic life between ANL-B1 and LANL-B2 was similar to that observed in the fatigue tests without holding. The ORNL-B1 sample however, exhibited greater cyclic hardening, reaching to a stress level similar to that of the ANL-B1 sample. This resulted in the longest cyclic life among the three AM builds.

For the SR samples, all three builds showed similar initial stress levels at the beginning of creep-fatigue tests. Although the ANL-B1 build was slightly harder than the LANL-B2 and ORNL-B1 builds, the differences in their initial strengths were minimal. All three AM builds experienced a brief period of cyclic hardening, followed by an extended phase of softening. The final cyclic lives were somewhat comparable among these builds. For the HIP samples, the stress responses of the ANL-B1 and ORNL-B1 builds were similar. Again, the initial strength of ANL-B1 was higher, but the ORNL-B1 build hardened to the same level as ANL-B1, resulting in a cyclic life approximately twice as long.

Based on the cyclic test results to date, the initial peak stress level of an AM build appears to be a good indicator of its cyclic performance compared to other AM builds, regardless of the applied post-heat treatment or hold time. The SA and HIP treatments significantly reduce the initial strength of AM materials, resulting in substantial cyclic hardening. A lower initial strength generally leads to a longer cyclic life, as shown in Figure 5.13a, b, d. The SR treatment also slightly reduces the initial strength of AM builds, but the effect is much weaker. Consequently, the cyclic lives of different AM builds are similar.

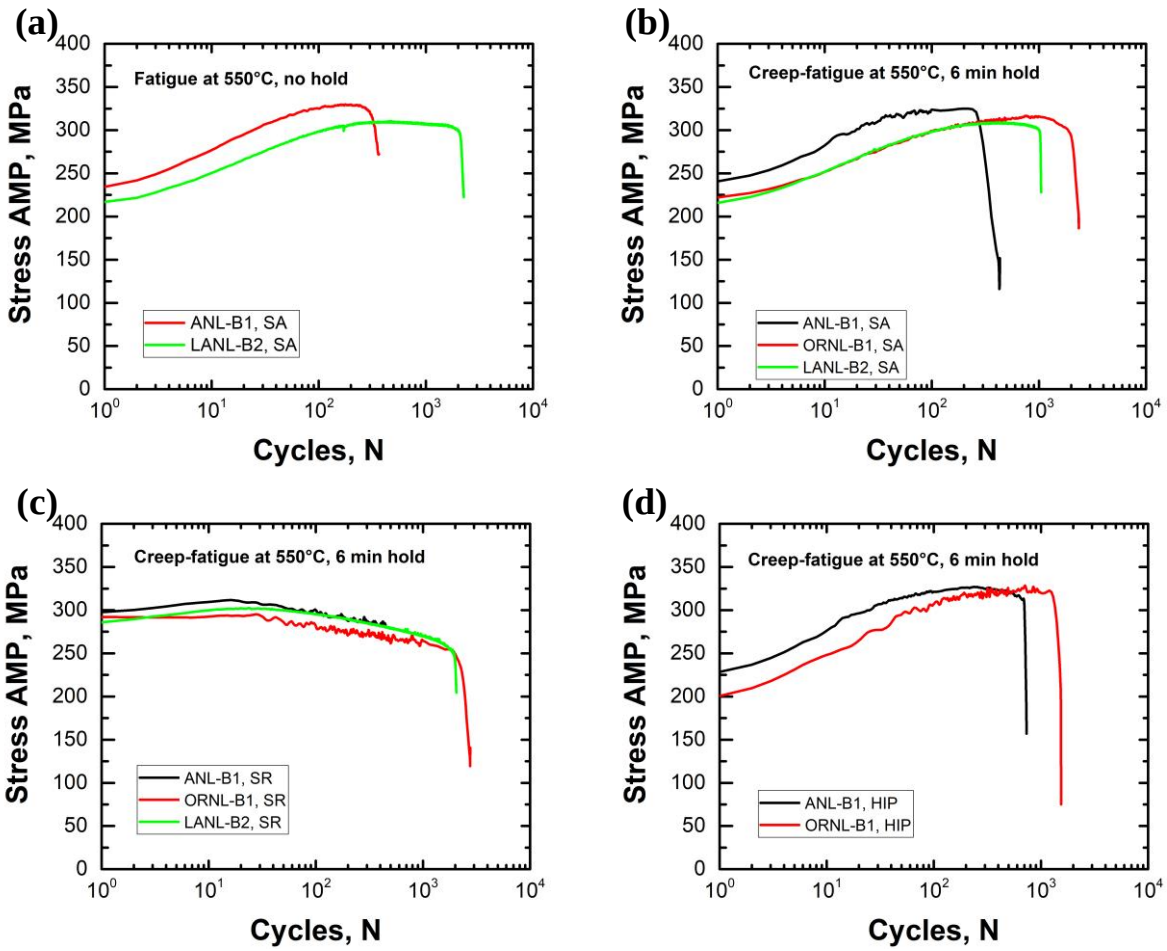

Figure 5.13 Stress-amplitude profiles of different AM builds tested at 550°C for fatigue (a), and creep-fatigue (b), (c), (d) on SA, SR, and HIP samples, respectively.

Currently, all cyclic tests performed on AM 316H builds are limited to a strain amplitude of 0.5%. To assess the impact of strain amplitude, these results are compared with a strain-life dataset on AM 316L SS in Figure 5.14. These AM 316L specimens were in their as-built condition, and were cyclically tested at 550°C without holding for a range of strain amplitudes below 0.5%. Most of the AM316H fatigue data points (i.e. the open triangle symbols in the figure) fall within the scatter band of AM316L SS (dashed lines in the figure), suggesting similar cyclic behavior between AM316L and AM316H, despite their differences in carbon content. One SA AM316H sample shows a somewhat worse fatigue life than the others. Nonetheless, the effects of post-build treatments are less evident in the creep-fatigue tests. For each AM316H build, the SR samples

perform better than the SA samples. The situation becomes complicated when all AM 316H builds are compared. The overall scatter is large. The ORNL-B1 build generally outperformed both LANL-B2 and ANL-B1 builds, suggesting that printing conditions, rather than the post-build heat treatment, play a critical role in the creep-fatigue performance of AM 316H SS.

A common observation from these AM316H tests is that, given the same post-build heat treatment, a lower initial strength generally results in a longer cyclic life regardless of hold time. Additional cyclic tests are needed to further explore the strain-life relationship of AM 316H, and the dependence of cyclic performance on printing and heat treatment conditions.

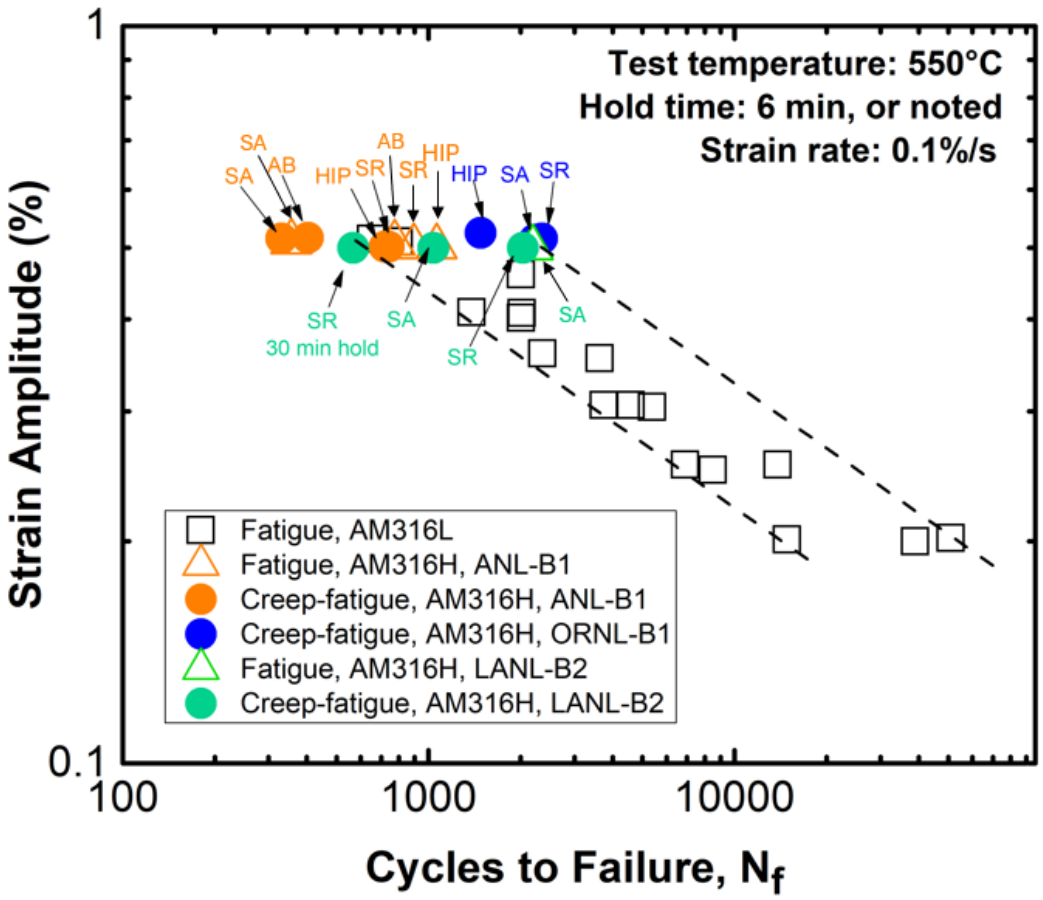

Figure 5.14 Cyclic performance of AM316H and AM 316L SSs.

6 Conclusion and outlook

The comprehensive mechanical tests in FY 24 on LPBF 316H SS manufactured on different machines, using various laser processing parameters, with variations on chemistry and post-build heat treatment, and with variations on specimen geometries has led to the following conclusions:

- The AB and SR materials exhibit similar behavior under tension and creep, as do the SA and HIP materials.
- In tension, the LPBF materials have higher YS but similar UTS compared to the wrought materials. The AB and SR LPBF materials are softer but more ductile than the SA and HIP LPBF materials.
- In creep, the LPBF materials have comparable rupture times but lower rupture strains compared to the wrought materials. The AB and SR LPBF materials have particularly low creep rupture strains (<10%) when tested at 720°C and 800°C. The SA and HIP materials are much more ductile than the AB and SR LPBF materials.
- The LPBF materials exhibit large scatter in fatigue and creep-fatigue lives. The cyclic lives of creep-fatigue tests are significantly lower than those of fatigue tests. As the temperature and hold time increase, the effect of creep damage becomes more pronounced.
- In fatigue and creep-fatigue, SR materials outperform SA materials in terms of cyclic lives.
- A common observation from the cyclic tests is that, given the same post-build heat treatment, a lower initial peak stress value generally results in a longer cyclic life regardless of hold time.
- In general, the batch variation can be more impacting than heat treatment, as demonstrated by the overall better performance of ORNL-B1 compared to ANL-B1.

In FY 25, efforts will be made in the following areas:

- Continue and complete the scoping tests with various batches of materials subjected to different heat treatment.
- Study the root cause of low creep rupture strains in SR materials and investigate in mitigation strategies.
- Optimize the grain structure (columnar vs. V-shaped) along with other microstructural features towards optimized performance.
- Start building the code case with SA materials.
- Perform mid-to-long term creep rupture tests.
- Perform tests on specimens with as-printed surfaces.

Acknowledgments

The work of the Argonne authors was sponsored by the U.S. Department of Energy, under Contract No. DE-AC02-06CH11357 with Argonne National Laboratory, managed and operated by UChicago Argonne LLC. Work performed at the Center for Nanoscale Materials, a U.S. Department of Energy Office of Science User Facility, was supported by the U.S. DOE, Office of Basic Energy Sciences, under Contract No. DE-AC02-06CH11357.

The work of the INL authors was sponsored by the United States (U.S.) Department of Energy (DOE) under Contract No. DE-AC07-05ID14517 with Idaho National Laboratory (INL), which is managed and operated by Battelle Energy Alliance.

The work of the ORNL authors was sponsored by the United States (U.S.) Department of Energy (DOE) under Contract No. DE-AC05-00OR22725 with Oak Ridge National Laboratory (ORNL), which is managed and operated by UT-Battelle LLC.

The authors acknowledge support for this work from the Advanced Materials and Manufacturing Technologies (AMMT) program with programmatic guidance provided by Meimei Li at Argonne National Laboratory, Ryan Dehoff at Oak Ridge National Laboratory and Dirk Cairns-Gallimore at the Department of Energy.

The authors thank Robin Montoya, Mark Messner, Peeyush Nandwana, Joel Simpson and Alex Pomo for technical supports, discussions and reviews.

Bibliography

[1] M. Li, D. Andersson, R. Dehoff, A. Jokisaari, I. van Rooyen, D. Cairns-Gallimore, Advanced Materials and Manufacturing Technologies (AMMT) 2022 Roadmap, Argonne National Lab. (ANL), Argonne, IL (United States), 2022. https://www.osti.gov/biblio/1958265 (accessed August 21, 2024).

[2] Standard Specification for Seamless Ferritic and Austenitic Alloy-Steel Boiler, Superheater, and Heat-Exchanger Tubes, (n.d.). https://www.astm.org/a0213_a0213m-22a.html (accessed August 20, 2024).

[3] P.C. Han, Q. Li, N.R. Tao, Strain partition induced abnormal low-cycle fatigue behavior in single-phase heterostructured 316L stainless steels, Scr. Mater. 227 (2023) 115274. https://doi.org/10.1016/j.scriptamat.2022.115274.

[4] M.C. Messner, X. Zhang, Y. Chen, C. Massey, M. McMurtrey, R.A. Montoya, M.J. Brand, O.R. Mireles, K. Le, Updated ASME design correlations and qualification plan for powder bed fusion 316H stainless steel, Argonne National Lab. (ANL), Argonne, IL (United States), 2024.

[5] E.H. Lee, P.J. Maziasz, A.F. Rowcliffe, Structure and composition of phases occurring in austenitic stainless steels in thermal and irradiation environments, Oak Ridge National Lab., TN (USA), 1980. https://www.osti.gov/biblio/5889791 (accessed August 20, 2024).

[6] J.K.L. Lai, A review of precipitation behaviour in AISI type 316 stainless steel, Mater. Sci. Eng. 61 (1983) 101–109. https://doi.org/10.1016/0025-5416(83)90191-X.

[7] B. Weiss, R. Stickler, Phase instabilities during high temperature exposure of 316 austenitic stainless steel, Metall. Trans. 3 (1972) 851–866. https://doi.org/10.1007/BF02647659.

[8] R.W. Hertzberg, R.P. Vinci, J.L. Hertzberg, Deformation and fracture mechanics of engineering materials, John Wiley & Sons, 2020.

Nuclear Science and Engineering Division
Argonne National Laboratory
9700 South Cass Avenue, Bldg. 212
Argonne, IL 60439

www.anl.gov